

THESIS FOR THE DEGREE OF LICENTIATE OF PHILOSOPHY

High Temperature Corrosion of Stainless Steels

The Effects of Chloride Salts and SO₂(g)

Sofia Karlsson



Department of Chemical and Biological Engineering
Chalmers University of Technology
Göteborg, Sweden 2011

High Temperature Corrosion of Stainless Steels

The effects of Chloride Salts and SO₂

Sofia Karlsson

© SOFIA KARLSSON, 2011.

Licentiatuppsatser vid Institutionen för kemi- och bioteknik
Chalmers tekniska högskola
Serie Nr. 2011:13
ISSN: 1652-943X

Department of Chemical and Biological Engineering
Chalmers University of Technology
SE-412 96 Gothenburg
Sweden
Telephone + 46 (0)31-772 1000

sofia.karlsson@chalmers.se

Cover: Backscattered electron image of a 304L sample exposed for 24 hours in the presence of KCl at 600°C in 5% O₂ and 40% H₂O.

Chalmers Reproservice
Gothenburg, Sweden, 2011

Abstract

The high corrosion rate of superheaters in waste- and biomass- fired plants is often linked to the presence of alkali chlorides. One way to mitigate the corrosion is to replace the superheater material with more corrosion- resistant materials. Another way is to change the corrosive environment by introducing fuel additives. In both cases it is important to know as much as possible about the corrosion process.

This study, investigates the corrosive effect of alkali chlorides and the beneficial effect of using sulphur-containing additives by laboratory and field exposures. In the laboratory study, the influence of three chloride salts, KCl, NaCl and CaCl₂, on the oxidation of 304L type (Fe18Cr10Ni) austenitic stainless at 600°C in O₂ + H₂O is investigated. The effect of sulphur is tested by adding 300 ppm SO₂ to the KCl exposure. In the field study the effect of sulphur is investigated by adding sulfur-rich municipal sewage sludge to the fuel which is rich in alkali and chlorine.

The laboratory results show that KCl and NaCl strongly accelerate the high temperature corrosion of 304L. The corrosion attack is initiated by the formation of alkali chromates through the reaction of alkali with the protective oxide. Chromate formation is a sink for chromium in the oxide; this leads to a loss of its protective properties. In contrast to NaCl and KCl, CaCl₂ is not very corrosive under the exposure conditions tested. CaCl₂ is rapidly converted to CaO and only small amounts of CaCrO₄ were detected in areas where CaO was in direct contact with the scale. The addition of SO₂ to the gas results in a drastic reduction of the corrosion rate of the KCl treated samples. The corrosion mitigating effect of SO₂ in this environment is attributed mainly to the rapid conversion of KCl to K₂SO₄. Unlike KCl, K₂SO₄ does not deplete the protective oxide in chromium by forming K₂CrO₄. It is also suggested that the formation of a thin sulphate film on the oxide surface impedes chromium volatilization in O₂ + H₂O environment and that it may decrease the rate of oxygen reduction on the oxide surface. The field study shows that the addition of sulphur rich material to the fuel mitigates corrosion in the superheater region of the power plant. Without additives, a thick corrosion product layer formed and the deposit was dominated by alkali chlorides. With additives, the amount of alkali chlorides in the deposit layer was very low and the steel was protected by a thin oxide. It is concluded that the beneficial effects of sulphur observed in the field can be explained in analogy to the lab experiments.

Keywords: Alkali induced corrosion, Sulphur additives, Biomass, Waste, Stainless Steels

List of publications

The thesis is primarily based on the work contained in the following appended papers, referred to by roman numerals in the text.

Paper I

S. Karlsson, J. Pettersson, L.-G. Johansson and J.-E. Svensson
Alkali Induced High Temperature Corrosion of Stainless Steel – The Influence of NaCl, KCl and CaCl₂
Submitted to *Oxidation of Metals*, (2011).

Paper II

S. Karlsson, J. Pettersson, J.-E. Svensson and L.-G. Johansson
KCl-Induced High Temperature Corrosion of Austenitic Stainless Steel 304L – The Influence of SO₂
Material Science Forum, (2011), **696**, pp 224-229.

Paper III

S. Karlsson, J. Pettersson and L.E. Åmand
Reducing high temperature corrosion when burning waste by adding digested sewage sludge
Proceedings of *The Swedish-Finnish Flame Days*, International Flame Research Foundation, January 26–27, (2011), Piteå, Sweden

Statement of contribution

In Papers I and II, I made all of the exposures and the XRD, IC, SEM and EDX analyses and was the main author. In Paper I, J. Froitzheim and N. Folkesson prepared the cross section. In Paper III, I assisted with the exposures, made some of the XRD analyses, made all of the IC analysis, the SEM analysis of the cross sections and wrote the paper together with L.E Åmand.

Related work

The following papers and reports have also been published, but are not included in this thesis.

Herstad Svärd, S., Steenari, B.-M., Åmand, L.-E., Bowalli, J., Öhlin, J., Pettersson, J., Karlsson, S., Larsson, E., Svensson, J.-E., Johansson, L.-G., Davidsson, K., Bäfver, L., Almark, M.

”Measures for simultaneous minimization of alkali related operating problems, Phase 3”
Värmeforsk report, Report number: A08-817, (2010).

Pettersson, J., Svensson, J.-E., Skog, E., Johansson, L.-G., Folkesson, N., Froitzheim, J., Karlsson, S., Larsson, E., Israelsson, N., Enestam, S., Tuiremo, J., Jonasson, A., Arnesson, B., Andersson B.-Å., Heikne, B.

“KME-411 Evaluation of different fuel additives ability to master corrosion and deposition on steam superheaters in a waste fired CFB-boiler”
KME report, Project KME-411 (2010).

List of acronyms

BIB	Broad ion beam
BSE	Backscattered electron
EDX	Energy dispersive X-ray
FEG	Field emission gun
FIB	Focused ion beam
IC	Ion chromatography
RDF	Refuse derived fuel
SE	Secondary electron
SEM	Scanning electron microscopy/microscope
XRD	X-ray diffraction

Table of Contents

1. Introduction.....	1
2. Biomass and waste fuels for power generation	3
3. Oxidation theory	5
3.1. Oxide formation	5
3.2. Kinetics.....	6
4. Oxidation of stainless steels.....	9
4.1. Stainless steels.....	9
4.2. Solid oxides important in high temperature corrosion	10
4.3. Fireside corrosion	12
5. Experimental and analytical techniques	15
5.1. Laboratory furnace experiments.....	15
5.1.1. Sample Preparation.....	15
5.1.2. Furnace Experiments	16
5.2. Field exposures.....	17
5.3. Analytical techniques	19
5.3.1. X-Ray Diffraction (XRD).....	19
5.3.2. Ion Chromatography (IC)	20
5.3.3. Scanning Electron Microscope (SEM) & Energy Dispersive X-ray (EDX)....	21
5.3.4. Focus Ion Beam (FIB)	24
5.3.5. Broad Ion Beam (BIB)	25
6. Results and Discussion	27
6.1. Laboratory Exposures	27
6.1.1. The effect of chloride salts	29
6.1.2. The effect of SO ₂	37
6.1.3. Summary of laboratory exposures.....	43
6.2. Field exposures.....	44
6.2.1. The effect of municipal sewage sludge	44
6.2.2. Summary of field exposures	49
7. Conclusions.....	51
8. Acknowledgements.....	53
9. Reference List	55

1. Introduction

According to the Intergovernmental Panel on Climate Change (IPCC), there is strong evidence that most of the global warming observed over the past 50 years is attributable to human activities. It is also believed that human influence will continue to change the atmospheric composition throughout the 21st century. This may result in an increased global average temperature and the sea level is projected to rise due to melting of polar ice. The greenhouse gas making the largest contribution from human activities is carbon dioxide (CO₂) which is released into the atmosphere by the combustion of fossil fuels, such as coal, oil or natural gas. Emissions of CO₂ due to fossil fuel burning are believed to be the dominant influence on the trends in atmospheric CO₂ concentration. Technological options for reducing anthropogenic emissions of CO₂ include reducing the use of fossil fuels [1].

A way to reduce the emission of CO₂ is the use of renewable energy sources, e.g. waste and biofuels instead of fossil fuels. The production of electricity from biomass and waste-fired power plants is increasing all over the world. However, in comparison with fossil fuels, the combustion of waste and biofuels often leads to a very complex flue gas. Due to this, severe corrosion is often a problem in waste and biomass fired power plants. High temperature corrosion leads to fast degradation of the material in several parts of the boiler. To deal with the corrosion problems, the maximum steam temperature in the boiler is kept lower than in fossil fuel power plants. This reduces the corrosion rate, but also decreases the electrical efficiency. Hence, in order to reach acceptable corrosion rates with maintained or higher efficiency in the production of power in waste and biomass-to-energy boilers, corrosion mitigating techniques are needed. One possibility is to use materials with higher corrosion resistance. Another possibility is to make the corrosive environment less corrosive, e.g. by using fuel additives.

This thesis investigates the corrosive effect of three chloride salts, often found in fly ash from waste and biofuels, and the effect of increasing the SO₂ level in the flue gas on the corrosion rate. The work consists of a laboratory study and a field study. The laboratory study investigates the corrosive effect of potassium chloride (KCl), sodium chloride (NaCl) and calcium chloride (CaCl₂) on the austenitic stainless steel 304L (Fe18Cr10Ni) at 600°C. The possibility of changing the atmosphere, to reduce the corrosion rate, is investigated by adding sulphur dioxide (SO₂) to the gas flow. In the field study, the laboratory results are validated by investigating the corrosion mitigating effects of co-

combusting a sulphur-rich additive with an alkali chloride-rich fuel. The field exposures were conducted in a 12MW CFB boiler at Chalmers University of Technology, Göteborg.

2. Biomass and waste fuels for power generation

The worldwide energy supply is based on fossil fuels such as coal, oil and natural gas. However, rising energy prices, unstable markets and the release of CO₂ have led to a growing interest in using renewable fuels (biomass and waste). Sweden has made a radical change from fossil fuel to renewable fuels and the trend shows that the energy derived from biomass and waste will continue to increase. An example of this rapid change is the Händelö plant in Norrköping, Sweden, where the percentage of fossil fuels has decreased from 100% in 1992 to 4–8% in 2009 and is projected to be 3–4% in 2013. The change in fuel selection is shown in Figure 1.

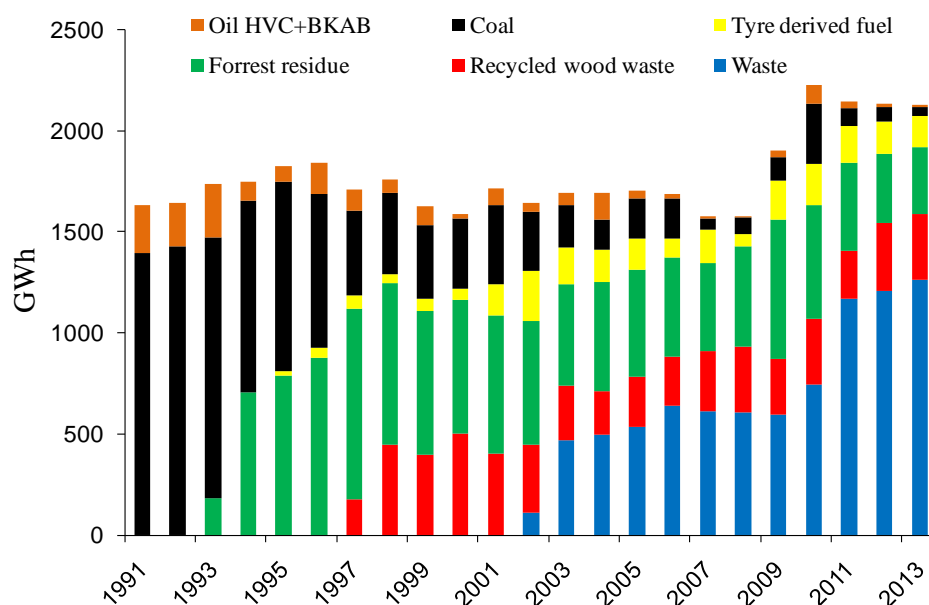


Figure 1. Power generation by fuel type at the Händelö plant in Norrköping, Sweden, from 1991 to 2013 [2]

Biomass fuels for heat and power generation can be divided into four primary classes: 1) wood and woody materials; 2) herbaceous and other annual growth materials such as straw, grasses, leaves; 3) agricultural residues; and 4) refuse-derived fuels (RDF) and waste or non-recyclable papers, often mixed with plastics. The fourth class is often excluded from the category of biomass, but the origin, with the exception of mixed plastics, justifies a classification as biomass [3]. Energy in a power plant is collected by heating water and subsequently steam by means of water walls, superheaters and economizers. The superheated steam enters the steam turbine, producing electric power. In addition hot water from the plant is used for district heating. In addition to the main components, (N₂ CO₂ H₂O and O₂) the flue gas produced when burning fossil fuels

contains high levels of sulphur dioxide (SO_2) and sometimes hydrogen chloride (HCl). In contrast, combustion of biomass and waste results in a flue gas with high amounts of alkali chlorides, while the concentrations of SO_2 are relatively low. The water content is generally higher when burning biomass and waste [4-6]. Hence, the deposits formed in the boilers are often rich in alkali chlorides which are known to cause accelerated corrosion, e.g. in the superheater region [4-11].

The steam superheaters are often affected by corrosion problems in power plants burning biomass and waste. Figure 2 shows a schematic illustration of the environment close to a superheater tube. During operation, a corrosion product layer forms on the steel tube. On top of this layer, a deposit is formed. Although the volume and composition of the deposit depends on the fuel composition, it is usually rich in chlorides and sulphates of alkali metals and calcium. Outside the deposit layer is the flue gas which consists of both gaseous species and particles. All of these phases and compounds may interact with each other, which makes the chemical environment on a superheater tube very complex.

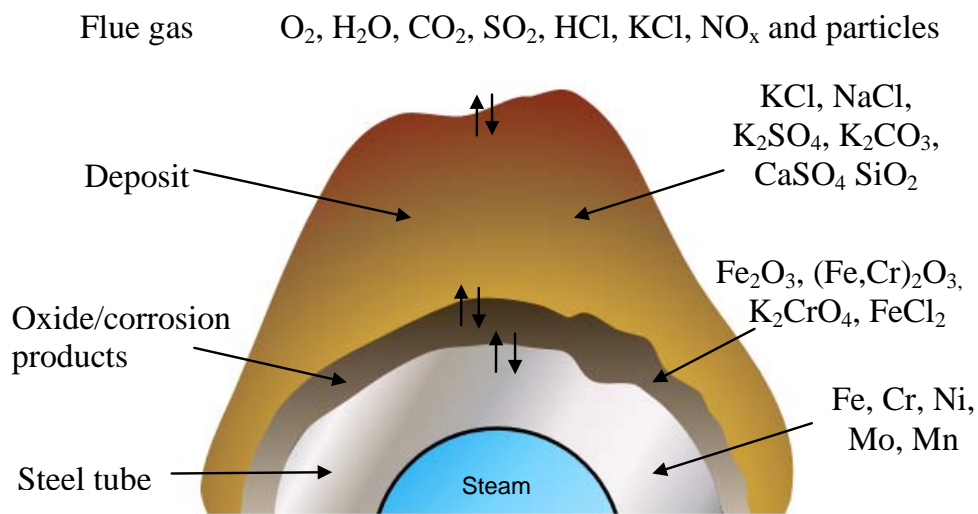


Figure 2. Schematic illustration of the complex environment close to the superheater in a biomass or waste fired boiler [12]

Due to the complex chemical situation close to the superheater tube, it is difficult to understand the causes behind the corrosion process. Therefore, it is also difficult to know how to prevent the corrosion problems. Hence, it is necessary to improve our knowledge of the corrosion processes in order to mitigate the corrosion problems. The present thesis aims to achieve this by a combination of simplified laboratory exposures and field studies.

3. Oxidation theory

3.1. Oxide formation

Most metals are thermodynamically unstable in environments containing oxygen and will therefore react to form oxides. The reaction rate increases rapidly with temperature and may cause problems of material degradation at high temperatures, e.g. in biomass and waste fired boilers.

Generally, an oxidation reaction is represented by the interaction of a metal with oxygen to form an oxide. The chemical reaction of a metal M and oxygen gas O₂ to form the oxide MO may be written as:



The oxidation process can be divided into three steps, see Figure 3. In the first step (a), oxygen is absorbed and then dissociate on the clean metal surface, followed by a charge transfer and the formation of O²⁻. In the second step (b), individual oxide nuclei form. The nuclei grow laterally on the surface until a continuous film is formed. In the third step (c), the surface oxide separates the metal from the gas and the reaction can then only proceed by solid state diffusion of the reactants through the film. The diffusion rate through the oxide is temperature dependent and at room temperature the diffusion rate is close to zero. However, increasing the temperature raises the diffusion rate and the oxide starts to grow [13].

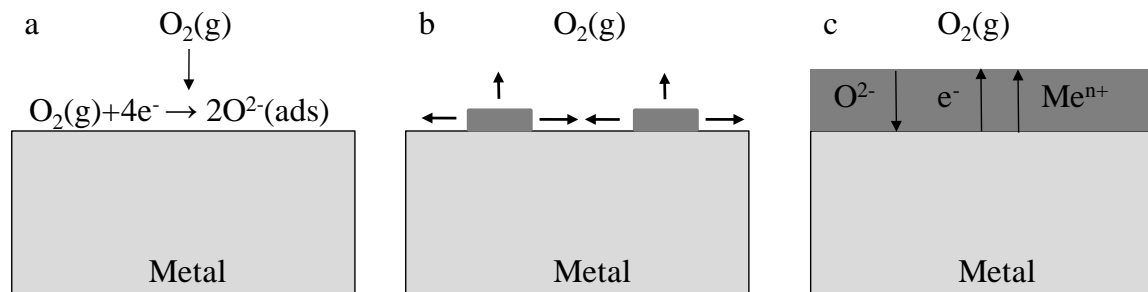


Figure 3. The initial formation of an oxide scale by adsorption of oxygen, oxide nucleation and growth to form a continuous oxide scale (stages a–c).

3.2. Kinetics

During oxidation a metal sample continuously increases in weight. This weight gain is due to the reaction ($M(s) + O_2 = MO_2(s)$) when the metal oxide forms. A common way to follow and study the oxidation rate is by measuring the weight change of the metal as it reacts with the gas. This kind of study gives information about the reaction mechanism and the rate-limiting step of the total reaction. Rate equations that are commonly encountered are linear, parabolic and logarithmic behaviour, all three represented in Figure 4. Important to remember is that the laws are derived from highly idealized models that often describe only a part of the oxidation behaviour.

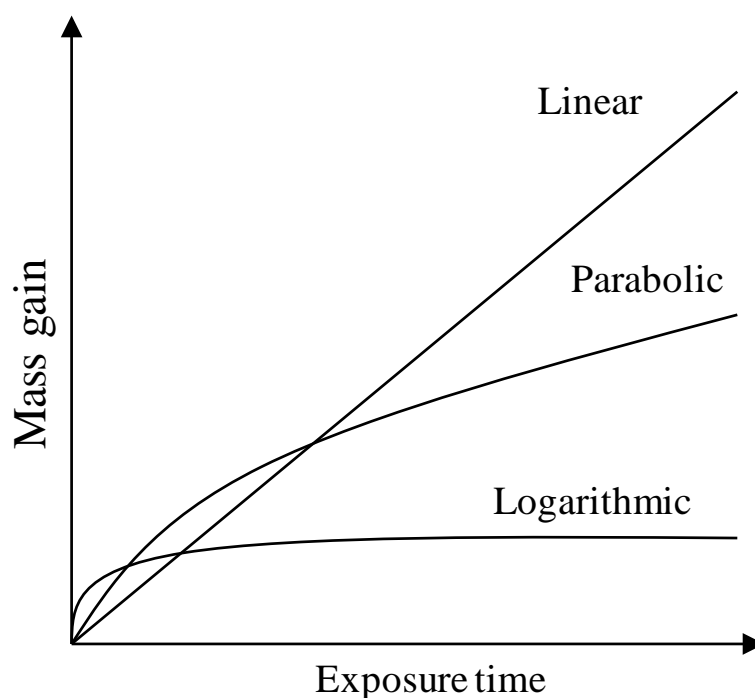


Figure 4. Mass gain versus exposure time for linear, parabolic and logarithmic growth.

Parabolic kinetics

With parabolic kinetics the oxide growth is fast during the initial stage and decrease with time. Most metals and alloys show parabolic rate at high temperatures [14]. The model for parabolic kinetics is mathematically expressed as:

$$x^2 = k_p t + A \quad (2)$$

where x = oxide thickness, k_p = parabolic rate constant, t = time and A = integration constant.

According to Wagner [15], the rate controlling step for oxide growth on a metal is the lattice diffusion of reaction atoms, ions or electron through the oxide layer; as the oxide layer grows thicker, the corrosion rate decreases. In his theory, Wagner derived an expression for k_p in terms of the electronic and ionic conductivity of the oxide [13]. However, Wagner's model takes into account only the lattice diffusion of atoms, ions and electrons as the rate determining step. Therefore, the model is based on the following assumptions:

- The oxide layer is compact, single-phased and well adherent;
- The oxide shows only small deviations from stoichiometry;
- Oxygen solubility in the metal may be disregarded;
- Diffusion of ions and electrons must be the rate determining step; and
- Thermodynamic equilibrium is maintained at the two interfaces as well as in the oxide.

Linear kinetics

In contrast to the parabolic growth rate, linear growth rate is constant over time and is thus independent of the amount of gas or metal previously consumed in the reaction. The rate determining step is therefore surface reactions or phase boundary processes [13]. Linear oxidation is mathematically expressed as:

$$x = k_1 t + B \quad (3)$$

where x = oxide thickness, k_1 = linear rate constant, t = time and B = integration constant.

Linear corrosion is often called “breakaway corrosion” or “catastrophic corrosion” and applies when the oxide scale is porous and non-protective. In this instance the oxide scale does not function as a barrier layer for ions and electrons. Cracking and spallation of the scale may induce linear behaviour because new metal is continuously exposed to the atmosphere.

Logarithmic kinetics

Logarithmic growth is most common at temperatures below 400°C [16]. Logarithmic growth is mathematically expressed as:

$$x = k_{\log} \log (t + t_0) + C \text{ (direct logarithmic law)} \quad (4)$$

$$x = D - k_{il} \log t \text{ (inverse logarithmic law)} \quad (5)$$

where x = oxide thickness, t = time, k_{\log} and k_{il} = rate constants and C and D = constants.

There are several of theories to explain the two logarithmic laws. These are based on various rate-determining mechanisms, e.g. transport of electrons or ions due to electric fields in or across the oxide film [13].

Combinations of rate equations

Oxidation processes often follow different laws at different stages of oxidation. An example is a thin protective oxide (parabolic behaviour) which transforms into a non-protective oxide (linear behaviour). This behaviour is usually called breakaway oxidation and is shown in Figure 5.

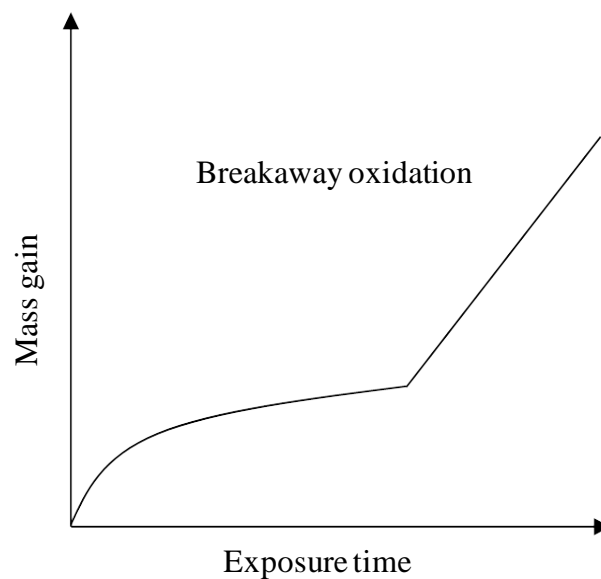


Figure 5. Typical mass gain curve for high temperature alloys suffering from breakaway oxidation.

4. Oxidation of stainless steels

4.1. Stainless steels

The addition of carbon to iron is sufficient to form steel. The presence of small amounts of carbon has a great strengthening effect on iron [17]. By adding chromium to the steel, the corrosion resistance is greatly improved. Stainless steels are iron-base alloys that contain a minimum of 11% chromium [18]. The corrosion resistance of stainless steels comes from their ability to form a chromium rich oxide film that grows slowly and protects the material from further oxidation.

Stainless steels can be classified into three groups by their crystalline structure: ferritic, martensitic and austenitic steels. Ferritic stainless steels have a body centred cubic (bcc) crystal structure (Figure 6a) and are ferromagnetic. Martensitic stainless steels have a body centred tetragonal (bct) crystal structure (Figure 6b) and are also ferromagnetic. The third class, austenitic stainless steels have a face centred cubic (fcc) crystal structure (Figure 6c) and are non-magnetic. Austenite is stabilized by alloying elements such as nickel and manganese.

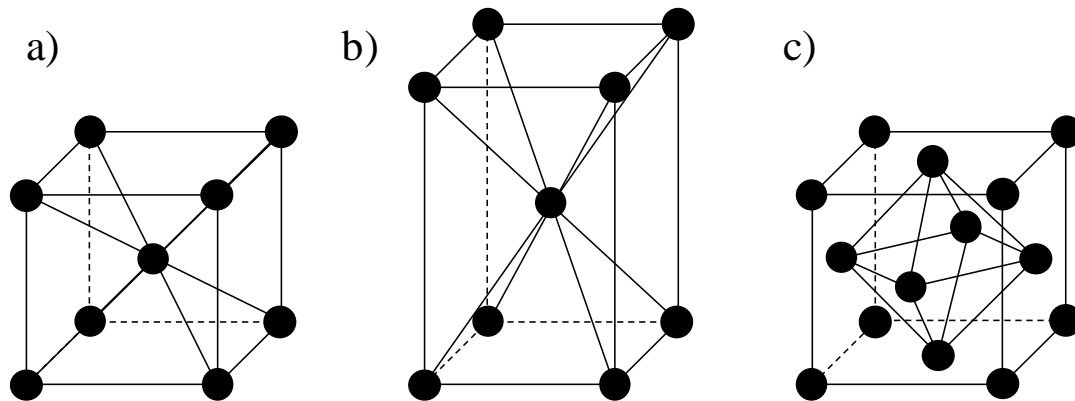


Figure 6. (a) body-centered cubic, (b) body-centered tetragonal and (c) face-centered cubic structure

Austenitic stainless steel: 304L and Sanicro 28

This thesis involves the austenitic stainless steel 304L (laboratory exposure and field exposure) and the high-alloyed austenitic stainless steel Sanicro 28 (field exposure). The material composition is presented in Table 1. 304L is a low carbon version of the more common 304 steel. The low carbon content prevents the formation of chromium carbides in the grain boundaries, which can deplete the steel in chromium. Sanicro 28 has a high chromium content and is commonly used in highly corrosive environments, e.g. superheater regions of boilers. Both steels are austenitic and known as chromia-forming alloys.

Table 1. Chemical composition of alloys 304L and Sanicro 28. Concentrations in weight percent and Fe in balance.

	Cr	Ni	Mn	Si	Mo	C
304L	18.47	10.12	1.19	0.36		0.012
Sanicro 28	26.68	30.56	1.77	0.42	3.39	0.014

4.2. Solid oxides important in high temperature corrosion

The corrosion resistance of a material is very dependent on what oxide may form at high temperatures. In high temperature oxidation of alloys, the scale generally consists of several oxide components. Oxides have different crystal structures, different ion diffusivities and differing capacity to resist corrosion attacks. The properties of the most important corrosion products are summarized in the follow sections:

Hematite, Fe₂O₃

Fe₂O₃ exists in two structures, α - Fe₂O₃ (hematite) and γ - Fe₂O₃. However, above 400°C only α - Fe₂O₃ is of importance [19]. α - Fe₂O₃ has the corundum type structure in which the oxygen ions form a hexagonal closed packed lattice with the cations located in two thirds of the octahedral sites. The oxide behaves as an n-type semiconductor in the temperature range 650–800°C and as p-type semiconductor at higher temperatures [13]. Hematite is the most protective of the iron oxides. However, in comparison to e.g., Cr₂O₃ it is considered to be poorly protective.

Magnetite, Fe₃O₄

Magnetite has the inverse spinel structure and contains both divalent and trivalent irons (Fe²⁺ and Fe³⁺). The structure consists of a face-centred cubic array of oxygen anions. Half of the trivalent ions occupy one eighth of the tetrahedral holes, and the rest of the ions occupy the octahedral holes. Magnetite is less protective than hematite; has a low degree of non-stoichiometry and behaves as an n-type semiconductor [13].

Wüstite, Fe_{1-x}O

Wüstite is stable above 570°C and is highly non-stoichiometric; its composition varying from Fe_{0.85}O to Fe_{0.95}O. The oxide has the rock salt structure with both the oxygen and iron ion sub-lattice of a cubic close-packed type. Wüstite is a p-type semiconductor with cation vacancies. Due to the high concentrations of defects, ionic transport in wüstite is very rapid, which means it is considered to be a non-protective oxide.

Eskolaite, Cr₂O₃

Eskolaite, or chromia, is the only solid chromium oxide which is stable at high temperatures. The structure is the corundum type and it is a p-type semiconductor. Solid-state diffusion is much slower than that of the iron oxides. Thus, Cr₂O₃ is one of the best protective oxides at high temperatures and the most protective oxide formed on stainless steels.

Corundum type solid solution, (Fe,Cr)₂O₃

Eskolaite, Cr₂O₃, is completely soluble in Fe₂O₃ and the oxide formed on stainless steels is usually a solid solution of both, i.e. (Fe_{1-x}Cr_x)₂O₃. The protectiveness of this type of oxide depends on its chromium content.

Spinel-type solid solution, (Fe,Cr,Ni)₃O₄

Oxides based on Fe, Cr and Ni may form solid solutions with a spinel type structure, e.g. (Fe,Cr,Ni)₃O₄. Compared to magnetite, some of the Fe(III) ions may be replaced by Cr(III) ions, whereas some of the Fe(II) ions may be replaced by Ni(II) ions. The actual composition depends on the abundance of Fe, Cr and Ni, as well as the oxygen activity in the oxide/metal interface. Spinel type oxides with other compositions may also form, e.g. (Fe,Cr)₃O₄ and (Cr,Mn)₃O₄.

4.3. Fireside corrosion

The flue gas produced when burning waste and bio fuels contains high amounts of water vapour and alkali chlorides. Previous laboratory results shows that both water vapour and alkali chlorides increase the corrosion rate of stainless steels at high temperatures. In the presence of water vapour, chromium is volatilized by the formation of chromic acid, $\text{CrO}_2(\text{OH})_2$, on the oxide surface [20-26]. Chromium volatilization depletes the protective oxide and the steel substrate in chromium. If the chromium content drops below a critical level, the oxide loses its protective properties and iron-rich oxide forms. The oxide is poorly protective and grows rapidly. The effect of water vapour on 304L at 600°C together with the mechanisms involved is given in the Chapter 6.

The corrosivity of alkali chlorides is often explained by the formation of volatile metal chlorides (e.g. FeCl_2 , CrCl_3 and NiCl_2) at the scale/metal interface. It has been suggested that the presence of metal chlorides significantly reduces the scale adhesion, which induces spallation of the corrosion product layer. Furthermore, transition metal chlorides are good ion conductors which accelerate the corrosion process. A mechanism commonly used to explain the corrosive effect of chlorine-containing compound is “active oxidation”, also known as the “chlorine cycle” [8-11, 27-29]. The mechanism supposes that chlorine (Cl_2) forms in a reaction between oxygen (O_2) and alkali chloride at the scale/metal interface. Chlorine then penetrates the scale and generates volatile transition metal chlorides at the scale/metal interface. The transition metal chlorides then diffuse back to the scale/gas interface where they are oxidized by O_2 , which releases $\text{Cl}_2(\text{g})$. It is suggested that the $\text{Cl}_2(\text{g})$ released then penetrates the oxide and reacts with the metal again, completing the cycle. Recently, a new, electrochemical mechanism was proposed to explain the alkali chloride-induced corrosion of low-alloyed steel. In the new mechanism, the chloride ion is the diffusing chlorine species rather than Cl_2 [30].

In contrast to the theory underlying the chlorine induced corrosion mechanism, previous laboratory results show that the potassium ion plays an important role in the initiation of KCl-induced corrosion of stainless steels [31-35]. Thus, it was shown that K_2CO_3 is equally corrosive as KCl towards stainless steel 304L at 600°C [36]. The corrosiveness of the potassium ion was attributed to the formation of potassium chromate by reaction with the oxide scale. The reaction depletes the oxide in chromium and destroys its protective properties. If any KCl is left on the surface after chromate formation, chlorine may penetrate the scale by anion diffusion and form transition metal chlorides at the

metal/oxide interface. In contrast to KCl and K_2CO_3 , the presence of K_2SO_4 does not increase the corrosion rate [36]. The non corrosive nature of K_2SO_4 at this temperature is explained by its inability to react with the protective, chromium rich oxide to form K_2CrO_4 . Thus, the corrosion resistance properties of the stainless steel remain intact. The effect of KCl on 304L at 600°C, together with mechanisms, is given in Chapter 6.

5. Experimental and analytical techniques

The aim of this work is to investigate the effect of chloride salts and SO₂ on the high temperature corrosion of stainless steels in biomass- and waste- fired boilers. The experimental approach has been to combine well-controlled laboratory exposures; to provide detailed corrosion mechanisms, and field exposures; to provide information about the about the corrosion process in the boiler. All samples, both laboratory exposures and field exposures, have been analyzed by detailed and advanced analytical methods in order to investigate the corrosion mechanisms.

5.1. Laboratory furnace experiments

The laboratory study explores the effect of three chloride salts on the high temperature corrosion of 304L. The study also includes an investigation the effect of adding SO₂ to the gas flow.

5.1.1. Sample Preparation

The material investigated is the austenitic stainless steel, 304L, the chemical composition of which is given in Table 1. The geometrical area of the samples was 5.56 cm², (15 × 15 × 2 mm). For handling, a hole ($\varphi = 1.5$ mm) was drilled, centred along one side of each sample. Before exposure the samples were ground with 320 grit SiC with deionized water. The samples were then polished with 9 μm, 3 μm and 1 μm diamond solution and lubricating liquid on a polishing cloth until a mirror-like surface was obtained. After polishing, the samples were degreased and cleaned in acetone and ethanol using an ultrasonic bath. The samples were coated with the preferred chloride salt (NaCl, KCl or CaCl₂) to a cation equivalent of 1.35 μmol/cm². The salts were applied by spraying the samples with a saturated solution of the preferred salt in water/ethanol. NaCl and KCl sprayed samples were weighed to calibrate the amount. Due to the hygroscopic nature of CaCl₂, the amount was calibrated with ion chromatography. The samples were dried with air and stored in a desiccator prior to exposure. The mass change of the samples was measured prior to and after exposure using a six decimal SartoriusTM balance.

5.1.2. Furnace Experiments

Laboratory exposures were carried out in horizontal silica tube furnaces. Two setups were used for the gas inlet, see Figure 7. Exposures in the absence of SO_2 were made in setup (a) and exposures in the presence of SO_2 were performed in setup (b). The atmosphere consisted of N_2 with 5% O_2 in all exposures. The flow rate was 2.5 cm/s and was controlled with a Bios DC2 Flow Calibrator. The dry gas was led through a humidifier and a temperature controlled condenser to obtain the correct water concentration (40%). In the SO_2 exposures, 300 ppm SO_2 were added directly to the furnace; the flow of SO_2 was controlled by a digital mass flow regulator. All exposures were isothermal and the temperature was kept at 600°C ($\pm 1^\circ\text{C}$). The samples were mounted three at a time using an alumina sample holder and positioned parallel to the gas flow direction. The experiment durations were 1, 24, 72 or 168 hours. Samples were weighed before and after exposure and all gravimetric measurements were made on a six decimal Sartorius™ balance. After exposure, the samples were stored in desiccators over P_2O_5 .

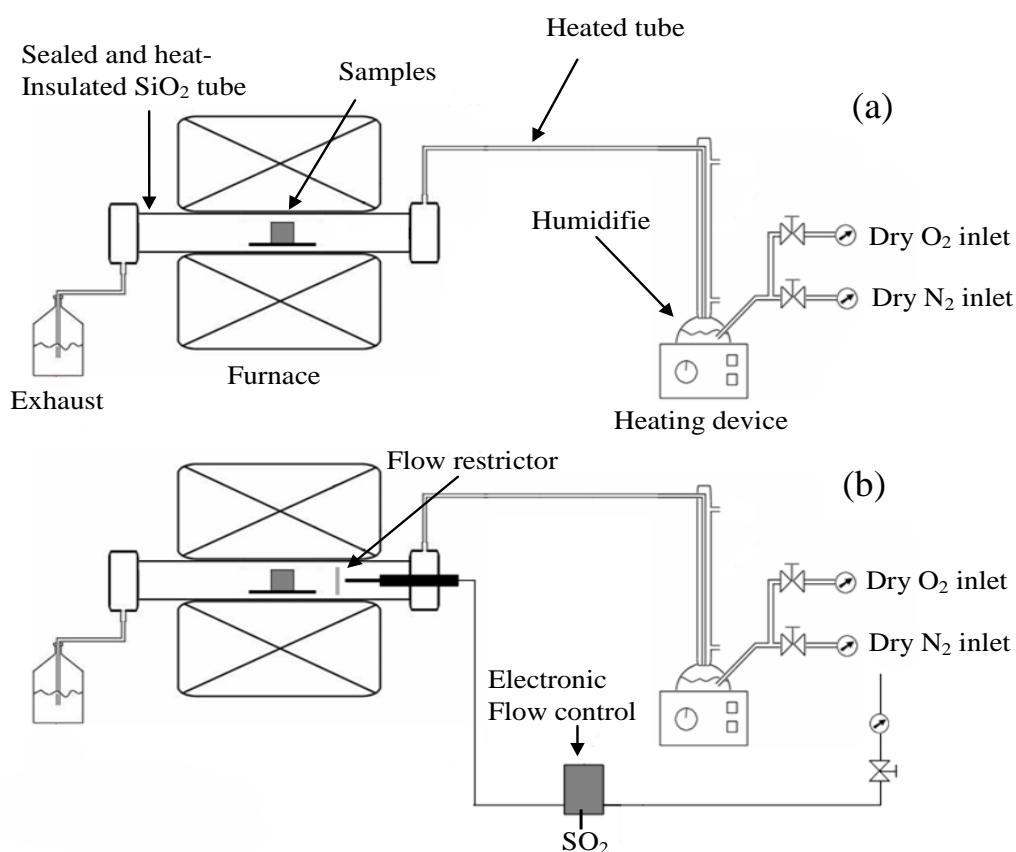


Figure 7. Horizontal tube furnace setups with gas inlet system for: a) dry and wet reference exposure and exposure in the presence of salt and b) dry and wet reference SO_2 exposure and SO_2 exposure in the presence of salt.

5.2. Field exposures

In the field study, the corrosion under normal operating conditions was characterized and the effect of adding municipal sewage sludge to the fuel on the corrosion mechanisms was investigated. The field exposures were carried out in a 12 MW circulating fluidized bed (CFB) boiler, located at Chalmers University of Technology, Göteborg (see Figure 8). The study included two different materials; 304L and Sanicro 28 (see Table 1 for composition). All samples had the form of rings with an outer diameter of 38 mm and a width of 15 mm.

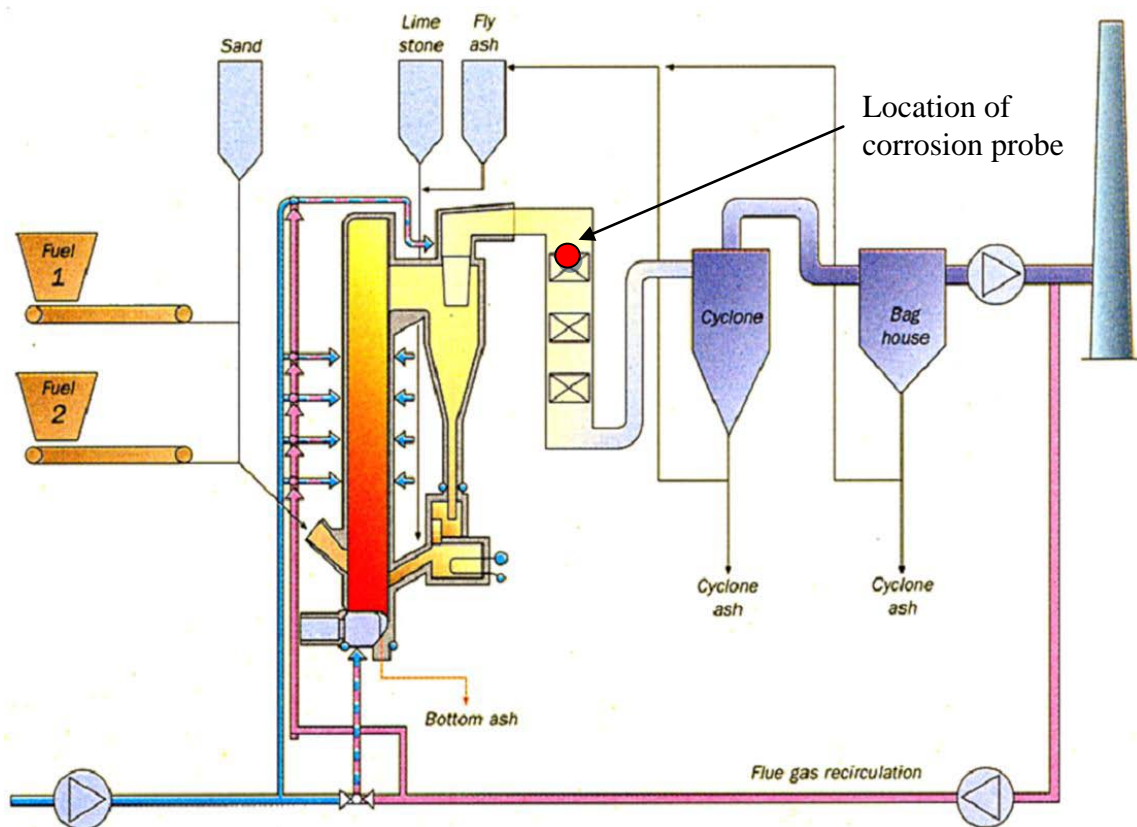


Figure 8. Schematic image of the research boiler at Chalmers University of Technology, Göteborg. Owned by Chalmers.

The exposures were made using a probe, constructed by Vattenfall (see Figure 9), which can expose two samples at three material temperatures (total six samples). Each sample had a thermocouple to enable the logging of individual material temperatures. The samples were mounted in such a way that the thermocouples were directed towards the gas stream, referred to as windward. Flue gas temperature at the probe position was approximately 820°C. The material temperature was controlled by adjusting the amount of cooled, pressurized air.

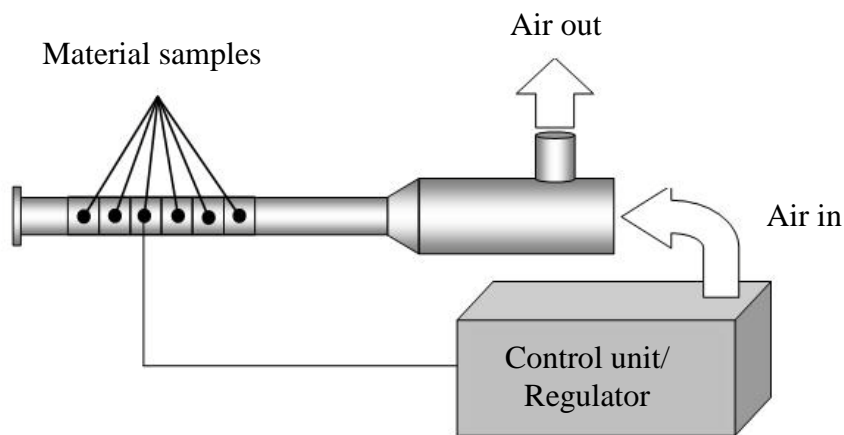


Figure 9. Schematic image of the corrosion probe used in the field exposures.

Three combustion cases were included in the study. In the reference case, denoted “RDF”, bark pellets were co-fired with waste (refuse derived fuel) pellets. The share of waste was 22% based on the total amount of dry fuel supplied to the boiler. In the “RDF-7%SJÖ” case, 7% municipal sewage sludge from *Sjölundaverket* was added to the “RDF” case. In the “RDF-13%HIM” case, 13% municipal sewage sludge from *Himmerfjärdsverket* was added to the “RDF” case. The flue gas composition was obtained by conventional instrumentation and an FTIR (Fourier Transform Infra Red spectrometry) instrument. Measurements of alkali chlorides (NaCl+KCl) were carried out by an IACM (*in situ* alkali chloride monitor).

This thesis includes the results from the “RDF” case and the “RDF-13%HIM” case. The material temperature was set to 600°C and the samples were exposed for 24 hours. Result from the “RDF-7%SJÖ” case is presented in paper III.

5.3. Analytical techniques

Numerous analytical techniques can be used to evaluate the exposed samples. All techniques have their advantages and drawbacks. To get a comprehensive view of the corrosion attack, it is important to use complementary techniques. In this chapter the different analytical techniques used in this work are presented.

5.3.1. X-Ray Diffraction (XRD)

Crystalline phases and corrosion products formed on the sample were analyzed with X-Ray Diffraction (XRD). The theory underlying the technique is that crystals are built up of planes each of which acts as a mirror (see Figure 10). When an X-ray beam strikes a sample, some of the X-rays are reflected by the plane at an angle of reflection equal to the angle of incidence. When Bragg's law is satisfied, the reflected beams are in phase and interfere constructively. Bragg's law is given by the following equation:

$$2d_{hkl} \sin \theta = n\lambda \quad (6)$$

where d_{hkl} is the distance between the planes in the crystal lattice, θ is the incidence/diffracted angle, n is an integer number, and λ the wavelength of the X-rays. At angles of incidence other than Bragg's law, reflected beams are out of phase and destructive interference or cancellation occurs.

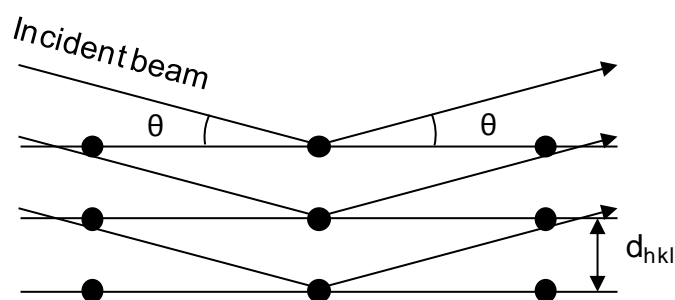


Figure 10. Illustration of diffraction by a series of crystal planes according to Bragg's law.

Each crystalline phase gives rise to a unique pattern of reflection at a specific angle. The data can be presented in a diagram with intensity as a function of the angle, 2θ . Identification is made by comparing the x-ray diffraction pattern obtained with a database. The intensity of the diffraction pattern is related to the concentration.

The most common set-up for the analysis of bulk materials is Bragg-Brentano geometry in which the source and the detector move symmetrically around the sample. In this work, grazing incidence X-ray diffraction (GIXRD) technique was used. This set-up facilitates the analysis of thin layers, e.g. oxide scales, since it has small incident angles for incoming X-rays. The small angle limits the penetration depth of the X-rays in the oxide scale and bulk material and allows the characterization of the usually thin oxide scales. Since the detector moves with the X-ray source at a fixed angle, the penetration depth of the X-ray can be changed from a few nm up to the μm range, see Figure 11.

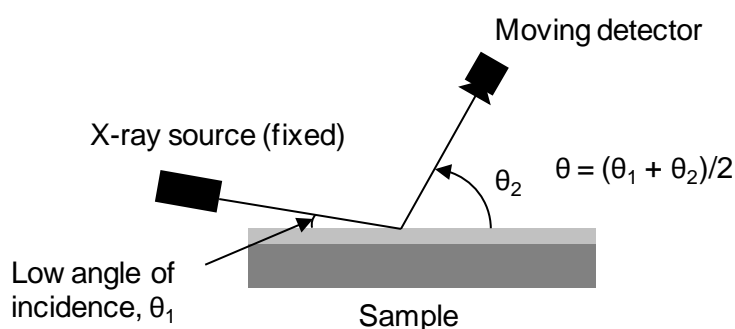


Figure 11. Setup for grazing incidence X-ray diffraction.

The instrument used in this study was a Siemens D5000 power diffractometer (Cu K_{α} radiation) equipped with a Göbel mirror and a grazing incidence attachment. Here, Cu K_{α} radiation was used and the angle of incidence was 1° – 5° . The detector measured between $20^{\circ} < 2\theta < 70^{\circ}$.

5.3.2. Ion Chromatography (IC)

The amount of water soluble ions in the corrosion product layer was determined by ion chromatography. In chromatographic separations, the sample ions are transported in a mobile phase. The phase is then forced through an immiscible stationary phase, which is fixed in a column. Those ions that are strongly retained by the stationary phases move very slowly with the flow of the mobile phase, while ions that are weakly held by the stationary phase move more rapidly. As a consequence of these differences in mobility, the ions become separated into discrete “zones” (see Figure 12a). Small, ions, such as chloride, will elute first from the column, while larger, divalent ions such as sulphates and chromates elute later. By placing a detector at the end of the column, the signals from the separated anions can be measured and plotted as a function of time (see Figure 12b). A

high concentration of a certain ion results in a high peak. The concentration of ions is then determined by comparing the detected signals with a standard solution of known concentration performance standards.

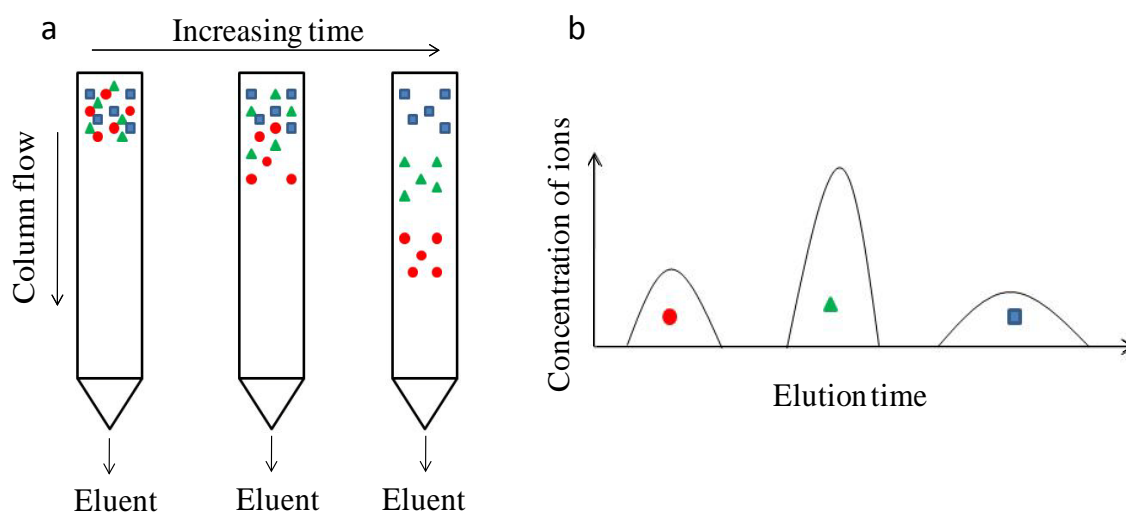


Figure 12. Schematic image of a) the ion separation in the column and b) signal of the detected ions.

In this work, the samples were first leached in MilliQ filtered water. To determine the amount of water-soluble anions (Cl^- and CrO_4^{2-} , SO_4^{2-}) a Dionex ICS-90 system was used. The anions were analysed with an IonPac AS4A-SC analytic column: a solution of 1.8 mM Na_2CO_3 /1.7mM NaHCO_3 was used as the eluent. To determine the amount of water-soluble cations (K^+ , Na^+ and Ca^+) a Dionex ICS-900 system was used. The cations were analysed with an IonPac CS12A analytic column and 20 mM sulfonic acid was used as eluent. The flow rate was 2mL/min for both anion and cation analyses.

5.3.3. Scanning Electron Microscope (SEM) & Energy Dispersive X-ray (EDX)

The Scanning Electron Microscope (SEM) was used for imaging and chemical analysis of the samples. The combination of high resolution and a large depth of focus enable a detailed study of the rough surface of the exposed samples. By connecting an energy dispersive X-ray (EDX) spectroscopy analysis system to the SEM, both qualitative and quantitative chemical analyses can be carried out.

The microscope operates by scanning a focused electron beam across the surface. When the high energy electrons strike the atoms in the sample, a variety of signals are generated, including secondary electrons, backscattered electrons, auger electrons and characteristic X-rays (Figure 13). All of the signals are generated in the entire interaction volume, but they are released from different depths according to their specific energy. This is illustrated in Figure 14.

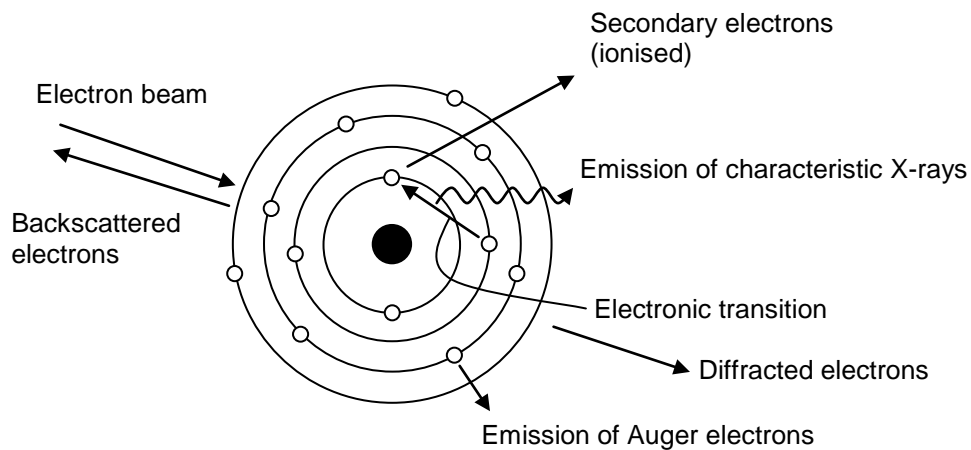


Figure 13. Some of the processes occurring in atoms when struck by high energy electrons [37].

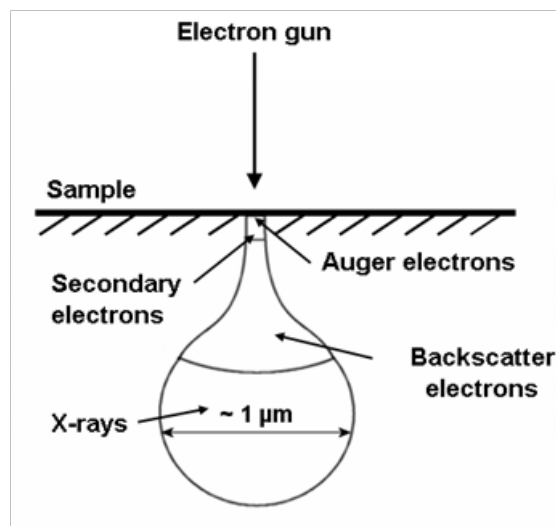


Figure 14. Illustration of the interaction volume in a material, showing the relative depth from which specific signals may escape.

In this work secondary electrons (SE) and backscattered electrons (BSE) are used for imaging and X-rays for chemical analysis. Secondary electrons are generated when incident beam electrons lose energy by inelastic collisions in the sample. Secondary electrons have low energy (<50 eV) and are generated close to the sample surface (<10nm). Therefore, a high resolution image can be obtained and the contrast in the image is determined by the topography of the sample.

Backscattered electrons are those from the primary electron beam that are scattered by the atomic nuclei in the sample. They have higher energies (>50 eV) than SEs and can therefore escape from a larger volume (0.1–0.5 μm deep), leading to a reduced resolution. The scattering of electrons by the nuclei implies a higher yield from heavier elements. The image therefore shows the distribution of the chemical compositions in the sample, where elements with high atomic number appear brighter than elements with a lower atomic number [38]. Figure 15 shows SEM images of a sample made by using (a) secondary electrons (SE image) and (b) back scatter electrons (BSE image).

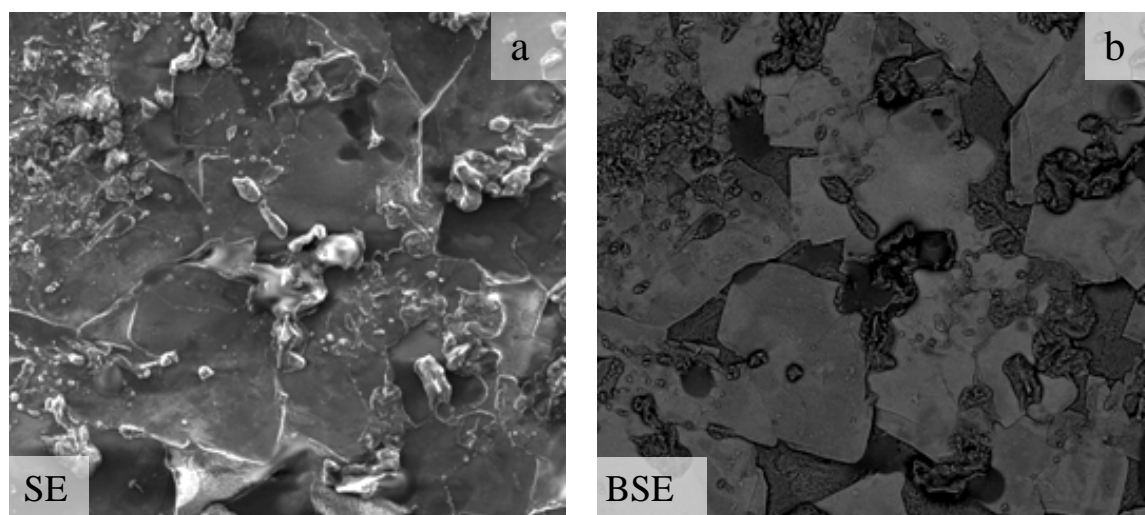


Figure 15. SEM images of a sample with (a) secondary electrons (SE image) and (b) back scatter electrons (BSE image)

The X-ray generated signals have an energy characteristic of the parent element and allow identification of the element. When the incident beam causes ionization by knocking out an electron from the sample atom, an empty low energy position is formed. As an outer electron relaxes into this position, X-rays are emitted. In the SEM, X-rays are used for chemical analysis, through an energy dispersive X-ray (EDX) detector. This provides rapid qualitative or (with adequate standards) quantitative analysis of elemental

composition with a sampling depth of 1–2 microns. These X-rays may also be used to form maps or line profiles, showing the elemental distribution in a sample surface. Figure 16 is an example of EDX mapping where (b) and (c) show the distribution of sodium (Na) and iron (Fe) on the sample surface showed the BSE image in (a).

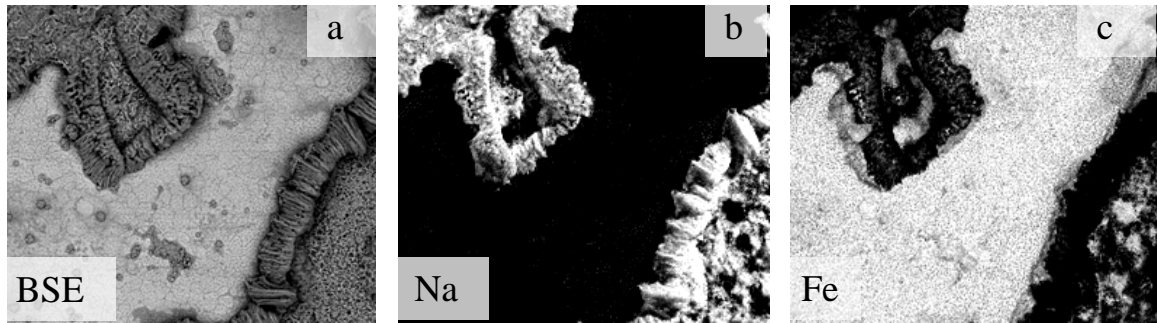


Figure 16. (a) BSE image of a sample surface together with EDX map of b) sodium and c) iron.

In this work an FEI Quanta 200 ESEM FEG was used. The ESEM was equipped with an Oxford Inca EDX system. The ESEM was operated in a high vacuum at 10–20 kV for imaging and at 12 kV for EDX analysis.

5.3.4. Focus Ion Beam (FIB)

The microstructure of the corrosion scales was investigated by examining cross sections prepared by Focused Ion Beam (FIB) milling. The FIB instruments operate similarly to SEM instruments, but they use gallium ions instead of electrons. The ions are used to mill away layers of the material from the sample surface. This results in a sharp cross-section, typically 10–40 μm across, of the oxide scale and the underlying metal.

The FIB cross-sections were prepared by using an FEI Strata 235 dual beam in a combined FIB/SEM system. The system was equipped with a liquid gallium ion source with a 30 kV accelerating voltage. A strip of platinum was deposited on the sample surface in order to protect it from damage during milling. The FIB cross sections were prepared by J. Froitzheim and N. Folkesson.

5.3.5. Broad Ion Beam (BIB)

The Focus Ion Beam is useful for a detailed investigation of a small area. To get a better overview of the scale, a wider cross section is necessary. With Broad Ion Beam (BIB) milling, wide cross sections in the millimeter range can be prepared. The BIB works in a similar way as a FIB but, instead of a focused gallium ion beam, a broad argon ion beam is used.

The BIB cross sections were prepared using a Hitachi E-3500 instrument and a Gatan Illion broad ion beam instrument. The ion guns were operated at 6kV, generating a broad ion beam. Consumable screens were positioned to protect most of the sample and render a smooth cross section. Prior to milling, a thin glass sheet was applied to the sample surface above a thin layer of epoxy. After hardening, the sample was cut (dry) using a low speed saw. The BIB cross sections were prepared and analysed by T. Jonsson.

6. Results and discussion

6.1. Laboratory Exposures

To determine the effect of different chlorine containing salts and sulphur dioxide ($\text{SO}_2(\text{g})$) in the presence of water vapour on 304L it is important to first investigate the oxidation properties in both dry and wet atmospheres. When exposed in a dry atmosphere, consisting of 5% O_2 (95% N_2 as carrier gas) at 600°C , 304L initially shows a very low mass gain (Figure 17). By extending the exposure time to 168 hours, the mass gain is more or less the same which shows that the oxide has a protective behaviour in dry atmosphere. Introducing 40% water vapour into the atmosphere changes the oxidation behaviour of 304L. In contrast to the protective behaviour in a dry atmosphere, the mass gain curve is linear during the first 168 hours, indicating that breakaway corrosion has occurred. After 168 hours of exposure, the mass gain is about 25 times larger than the corresponding exposure in dry air.

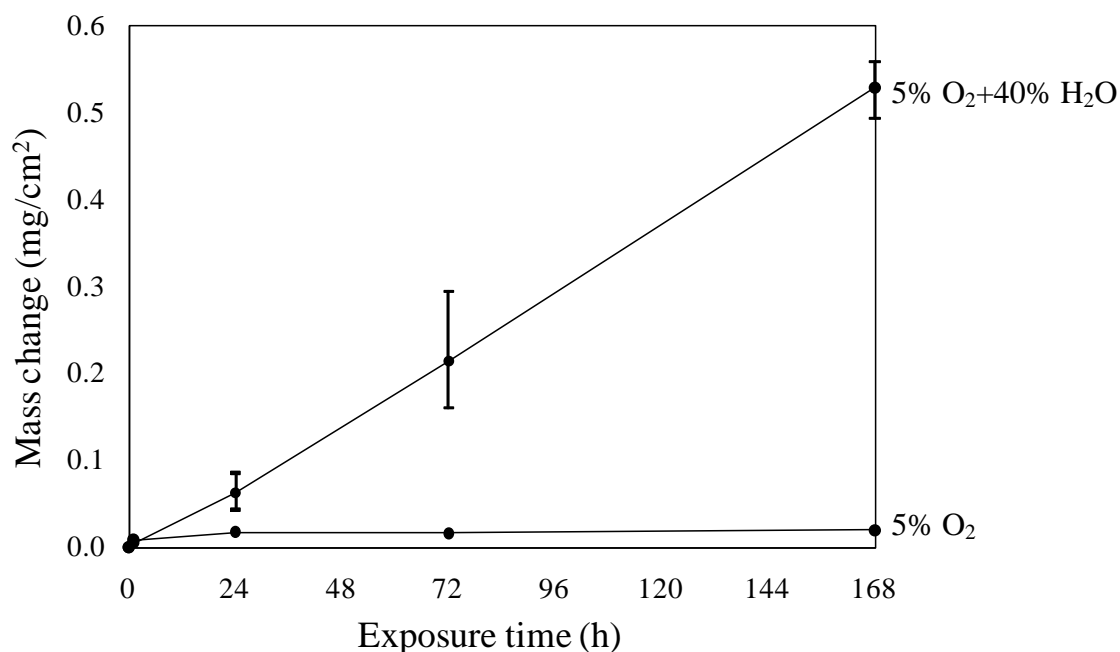


Figure 17. Mass gain versus exposure time for 304L samples exposed in O_2 and $\text{O}_2 + 40\% \text{H}_2\text{O}$ at 600°C [12].

The SE images in Figure 18 show the surface of samples exposed in (a) dry atmosphere and (b) wet atmosphere, both after 24 hours of exposure at 600°C . In the dry exposure a smooth Cr-rich protective scale has formed. Previous studies show that the oxide is a chromia rich corundum type oxide which reaches a thickness of $< 200\text{nm}$ after 168 hours

[20, 21, 39]. In the wet exposure the sample surface becomes covered by oxide islands. The majority of the work regarding the effect of water vapour on 304L has been presented earlier [20, 21, 23] and a mechanism has been suggested which states that water vapour destroys the protective oxide by depletion of chromium. The depletion is driven by the formation of gaseous chromic acid:



If the chromium content drops below a critical level, the oxide loses its protective properties and an iron-rich, rapidly growing oxide forms. Therefore, the supply of chromium to the oxide by diffusion in the metal must match the evaporation rate to maintain the protective properties of the oxide. At the alloy grain boundaries the diffusion is higher than at the centre of the steel grains. Hence, the oxidation behaviour of the steel surface depends on the distance to a grain boundary. This explains why “islands” consisting of thick oxide form on central parts of the steel grains while the areas close to a grain boundary retain a thin slow-growing oxide. The oxide islands are layered and consist of an outward growing hematite (Fe_2O_3) and an inward growing spinel-type ($(\text{Fe,Cr,Ni})_3\text{O}_4$) layer, separated by the former steel surface [40]. This two-layered scale is expected to be poorly protective and permeable for oxide and chloride ions which, if present, would further accelerate the corrosion rate.

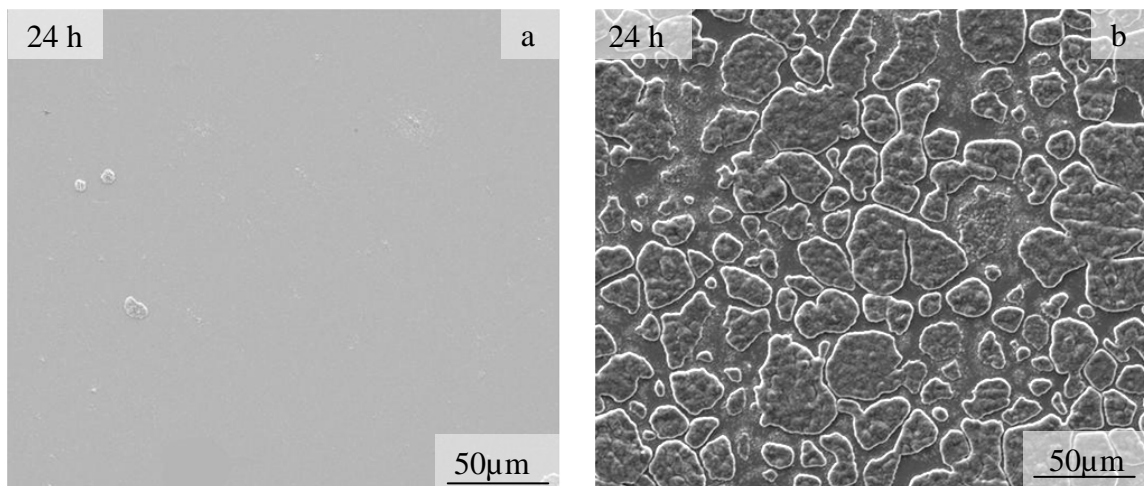


Figure 18. SEM images of 304L samples exposed in (a) 5% O₂ and (b) 5% O₂ and 40% H₂O for 24 hours at 600°C.

6.1.1. The effect of chloride salts

In general, any process that depletes the protective oxide and the steel substrate in chromium is expected to make the stainless steel more vulnerable to high temperature corrosion. It has been shown that KCl and K_2CO_3 increase the corrosion rate of 304L and Sanicro 28 by potassium chromate formation [31-36]. Chromate formation is a sink for chromium in the oxide; this leads to a loss of its protective properties. Combustions of waste and biofuels often results in deposits rich in potassium compounds. In addition, they are also rich in sodium and calcium compounds. Therefore, it is of great interest to investigate whether NaCl and $CaCl_2$, like KCl, cause accelerated corrosion.

To investigate the effect of NaCl and $CaCl_2$, a comparison with KCl has been made. Figure 19 shows mass gain versus time for samples exposed in the presence of KCl, NaCl and $CaCl_2$ in 5% O_2 + 40% H_2O at 600°C. Reference exposures in 5% O_2 and 5% O_2 + 40% H_2O are also included. The result shows that both KCl and NaCl strongly accelerate the corrosion of 304L. In contrast, exposure in the presence of $CaCl_2$ does not result in a significantly increased mass gain. The slightly lower mass gain of the $CaCl_2$ exposed samples, when compared with the salt free exposures, is not believed to be significant because of substantial scale spallation of the samples after the longer exposure times.

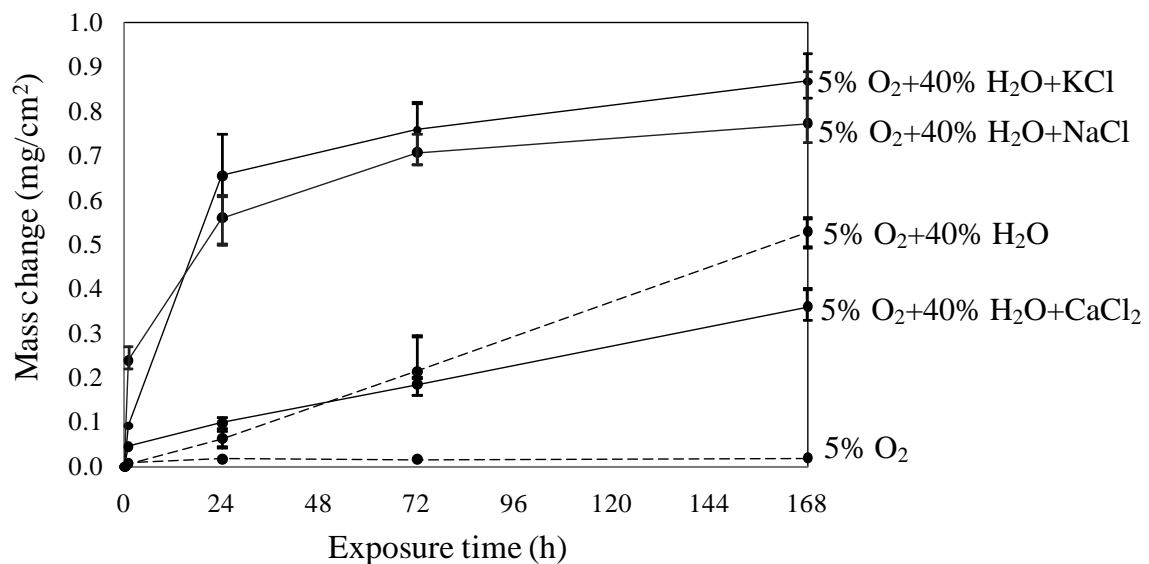


Figure 19. Mass gain versus exposure time for 304L samples exposed in the presence of KCl, NaCl and $CaCl_2$ in O_2 + 40% H_2O at 600°C. Reference exposures in O_2 and O_2 + 40% H_2O are also included.

To analyze and compare corrosion products formed during the salt exposures, the samples were investigated with X-ray diffraction (XRD) and ion chromatography (IC). Table 2 shows the results from the XRD analysis of the salt treated samples after 24 hours exposure. The results are similar for KCl and NaCl. In both cases, no unreacted salt was detected, suggesting that the salt has completely reacted after 24 hours. Alkali chromates (K_2CrO_4 and Na_2CrO_4) were detected on both KCl and NaCl treated samples. This indicates that NaCl does react with the protective oxide in a way similar to that of KCl. The XRD analysis also detected hematite (Fe_2O_3) and spinel type oxide (Me_3O_4), which indicates that the protective oxide has been converted to a poorly protective iron-rich oxide.

In contrast to the NaCl and KCl samples, the XRD analysis of the $CaCl_2$ treated sample shows no evidence of calcium chromate ($CaCrO_4$). Instead, calcium oxide (CaO) and dicalcium ferrate (III), ($Ca_2Fe_2O_5$) was detected which indicates that under these conditions $CaCl_2$ does not react in the same way as KCl and NaCl. Furthermore, both Fe_2O_3 and Me_3O_4 was detected which shows that an iron rich oxide has started to form. However, medium intensity diffraction from the steel substrate indicates that the oxide is still thin.

Table 2. Crystalline phases detected by XRD on 304L for 24 hours in the presence of KCl, NaCl and $CaCl_2$ in $O_2 + 40\% H_2O$ at $600^\circ C$

Salt	304L	Fe_2O_3	Me_3O_4	K_2CrO_4		
KCl	–	S	W	W		
NaCl	–	S	W	W		
$CaCl_2$	304L	Fe_2O_3	Me_3O_4	$CaCrO_4$	$Ca_2Fe_2O_5$	CaO

S= Strong intensity, M = Medium intensity, W = Weak intensity

In agreement with the XRD results, chromate ions were detected with IC analysis on both KCl and NaCl treated samples after 24 hours of exposure. For KCl treated samples, the amount of potassium ions found corresponds to the amount of chlorine ions and chromate ions detected. In contrast, the amount of sodium ions found on the NaCl treated samples exceeds the amount of chlorine ions and chromate ions. This indicates that other types of sodium compounds have formed. In the case of $CaCl_2$ small amounts of chromate ions

were detected. However, according to the XRD analysis, most of CaCl_2 forms CaO and $\text{Ca}_2\text{Fe}_2\text{O}_5$.

The surface morphology of the exposed samples was investigated by SEM. Figure 20 shows plan view SE images of the samples before exposure (top row) together with plan view BSE images after 24 hours of exposure (bottom row). After exposure, KCl and NaCl treated samples are covered by a thick scale and the salt crystals are replaced by irregularly shaped oxide agglomerations. The KCl treated sample exhibits island-like scale morphology, while the surface on the NaCl treated sample is very uneven. The CaCl_2 treated sample shows roughly circular areas corresponding to the salt deposited. As for to the KCl treated sample, the surface also exhibits island-like scale morphology. In contrast, the oxide islands seem to be much thinner, especially in areas between the former salt particles.

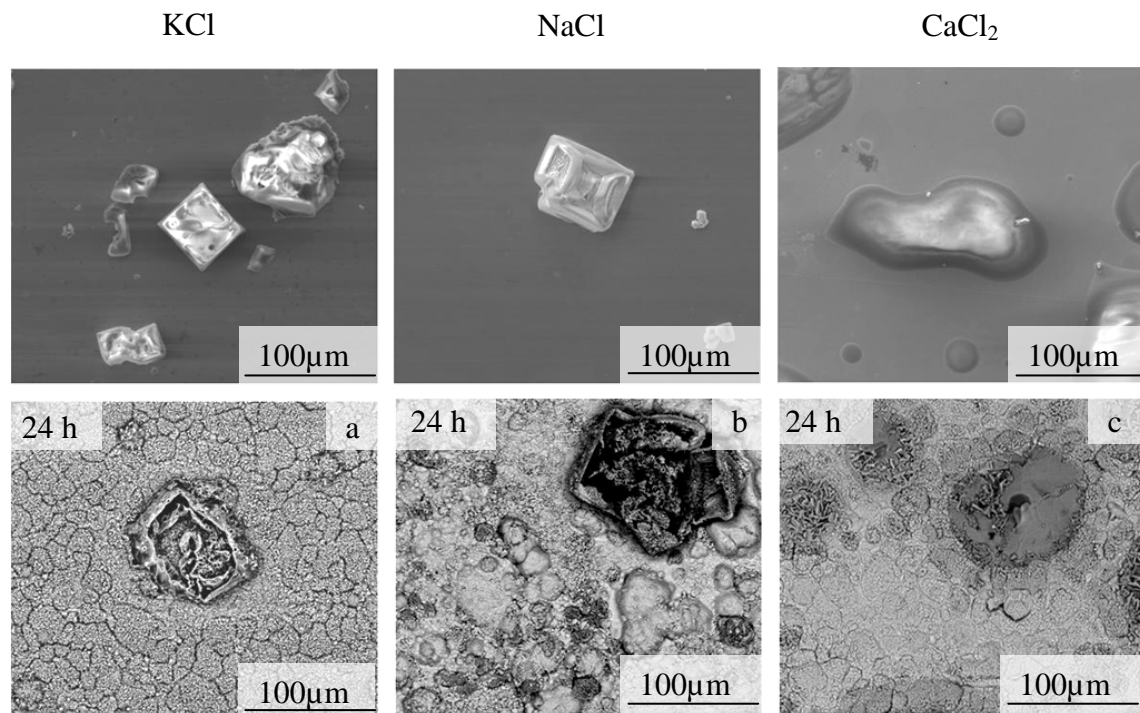
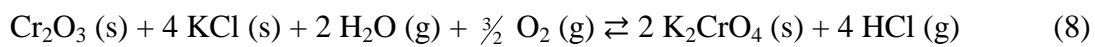


Figure 20. Top row: SE images of 304L samples with KCl, NaCl and CaCl_2 crystallites before exposure. Bottom row (a – b): BSE images of the same samples after 24 hours of exposure in 5% O_2 and 40% H_2O for 24 hours at 600°C.

The distribution of elements on the surface was analyzed with SEM/EDX. Figure 21 shows EDX maps of the KCl treated sample in Figure 20a. The analysis shows that the covering oxide is iron rich and, in agreement with XRD, no unreacted salt or chlorine is detected on the surface. Instead, potassium can be found in areas that correlate to chromium and oxygen in the EDX maps. K_2CrO_4 was identified by XRD on the KCl treated samples. Hence, these particles are attributed to K_2CrO_4 . K_2CrO_4 can be detected in the remains of the salt particle and on the oxide surface between these particles. Therefore, it is proposed that KCl diffuses out from the salt particle and, together with O_2 and H_2O , reacts with the protective chromium rich oxide that initially forms [32, 35]:



The reaction depletes the oxide in chromium, which results in a breakdown of the protective properties of the oxide and triggers the formation of a rapidly growing iron-rich scale. In addition, $HCl(g)$ is formed in the reaction. However, since no chlorine is detected on the sample, it is suggested that $HCl(g)$ leaves the surface with the gas flow.

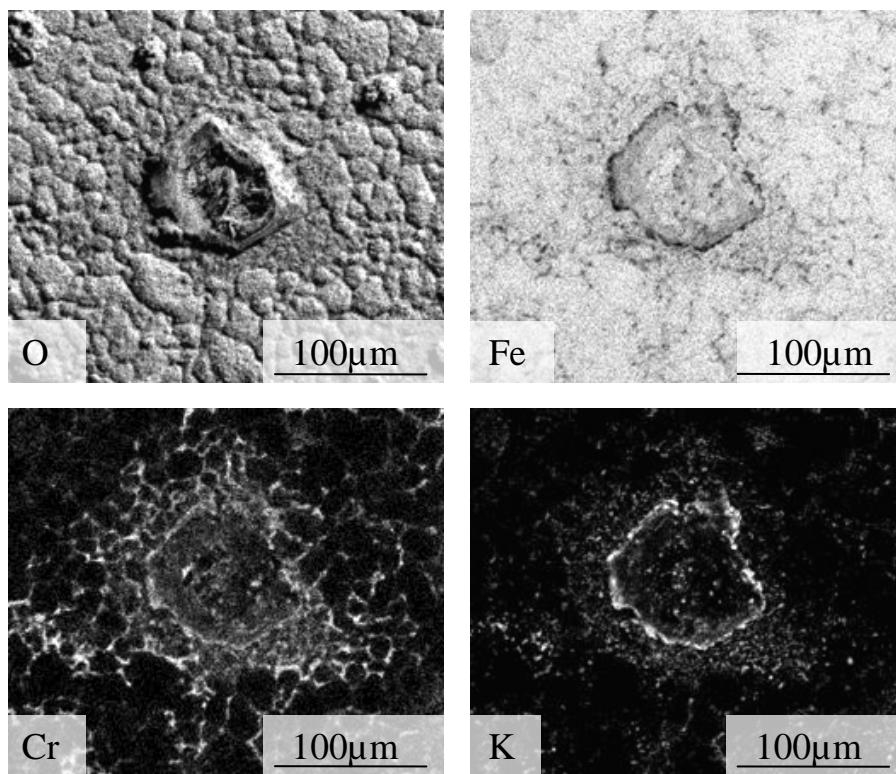
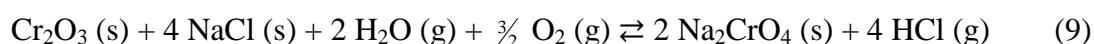


Figure 21. EDX images of a sample exposed for 24 hours in the presence of KCl at 600°C in 5% O_2 + 40% H_2O .

Figure 22 shows EDX maps of the NaCl treated sample in Figure 20b. The surface is covered by an iron rich oxide, and no unreacted salt or chlorine is detected. In similarity to KCl treated samples, sodium can be found in areas that correlate to chromium and oxygen in the EDX maps. On the NaCl treated samples Na_2CrO_4 was identified by XRD. Hence, these particles are attributed to Na_2CrO_4 . Na_2CrO_4 can be detected in the remains of the salt particle and on the surrounding oxide. In the same way as with KCl, NaCl seems to diffuse out from the salt particle and react with the protective oxide that initially forms:



In contrast to KCl exposed samples, EDX point analyses of NaCl treated samples also detected corrosion products in which sodium correlates to iron, possibly sodium ferrate(III), ($\text{Na}_2\text{Fe}_2\text{O}_4$). This is in agreement with the IC results showing that the amount of sodium exceeds the number of moles of chromate and chloride found. This is discussed in more Paper in Article 1.

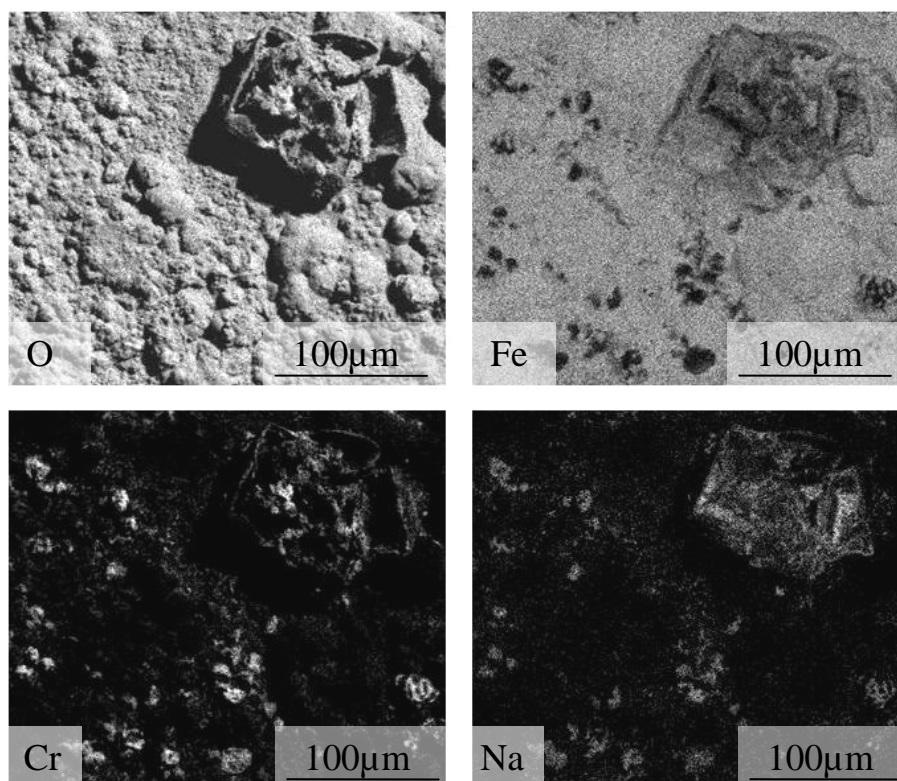


Figure 22. EDX images of a sample exposed for 24 hours in presence of NaCl at 600°C in 5% O_2 + 40% H_2O .

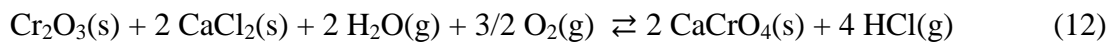
Figure 23 shows EDX maps of the CaCl₂ treated sample in Figure 20c. The area between the remains of the salt particles is partly covered by iron-rich oxide islands. The image shows a network pattern consisting of a thin chromium rich oxide scale, corresponding to the grain boundaries in the steel substrate. The presence of a thin oxide is in accordance with XRD where diffraction peaks with high from the steel substrate were detected. In contrast to the KCl and NaCl exposed samples, no calcium can be detected on the oxide surface. Instead, EDX mapping detects calcium, iron and oxygen in the patches that correspond to the original agglomerations of CaCl₂ particles. This is in agreement with XRD by which CaO and Ca₂Fe₂O₅ were detected. Therefore it is proposed that CaCl₂ is rapidly converted to CaO:



CaO may then react further with iron to form Ca₂Fe₂O₅:



Overlapping between Ca and Cr at the edges of the circular patches indicates the presence of CaCrO₄. This is in agreement with IC analysis by which small amounts of chromate ions were detected. CaCrO₄ may be formed by the reaction with the protective oxide and CaCl₂:



Due to the fast conversion from CaCl₂ to CaO, the reaction is limited. CaCrO₄ may also be formed by the reaction with the protective oxide and CaO:



However, because of the poor mobility of CaO, Ca does not spread over the surface and the reaction between Ca and the protective oxide is limited. Thus, the depletion of chromium by chromate formation is located in areas close to the remains of the salt particles, while the surface in between is unaffected by the salt.

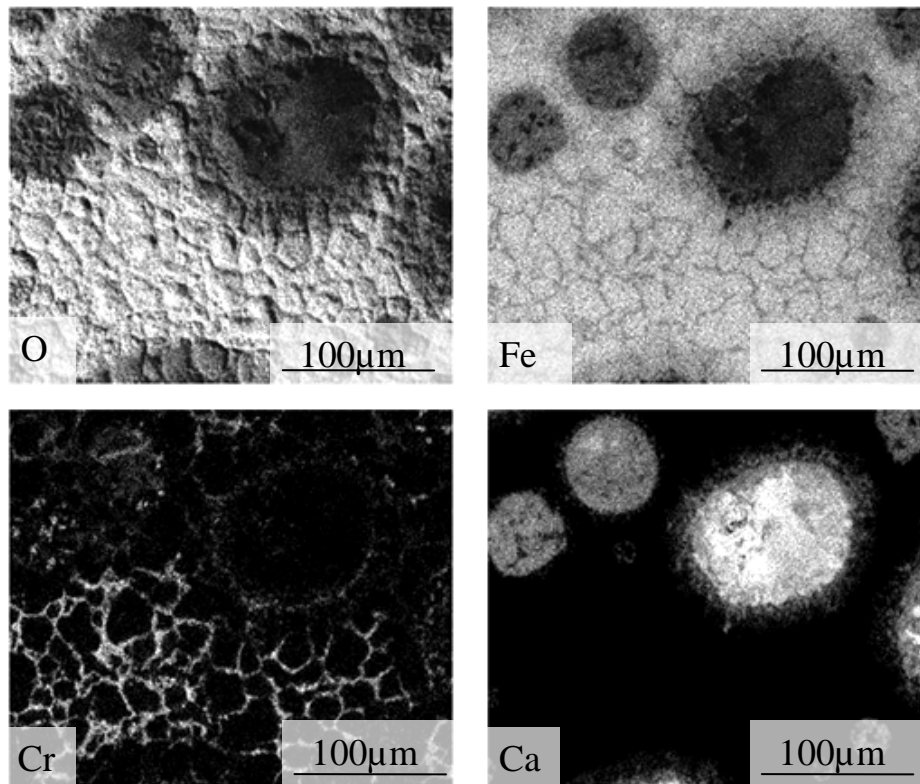


Figure 23. EDX images of a sample exposed for 24 hours in presence of CaCl_2 at 600°C in 5% O_2 + 40% H_2O .

To further investigate the oxide scale, FIB cross sections were prepared from samples exposed for 24 hours, see Figure 24a–c. The FIB cross section on the KCl treated sample was cut through the remains of the salt particle salt particle, Figure 24(a). The oxide scale is divided into an outward and an inward layer. The outward layer of the scale consists of almost pure Fe_2O_3 , while the inward layer consists of an iron, chromium and nickel oxide. Spinel type oxide was detected by XRD; previous studies have shown that the oxide is $(\text{Fe,Cr,Ni})_3\text{O}_4$ [35].

The FIB cross section of the NaCl treated sample, also cut through the remains of the salt particle, is shown in Figure 24(b). The result shows corrosion morphology similar to that on the KCl sample. Thus, a two layered oxide scale has formed beneath the former salt particle, consisting of an outward iron-rich layer (almost pure Fe_2O_3) and an inward layer containing iron, chromium and nickel (presumably $(\text{Fe,Cr,Ni})_3\text{O}_4$).

The FIB cross section of the CaCl_2 treated sample includes a part of the remains of the salt particle and the surrounding area; see Figure 24(c). The surrounding area shows similar oxidation morphology as observed in 5% O_2 + 40% H_2O environment in the absence of salt [40]. Again, it is suggested that the outward and inward layers are made up of Fe_2O_3 and $(\text{Fe,Cr,Ni})_3\text{O}_4$, respectively. The area formerly covered by salt exhibits a scale consisting of three distinctive layers. The outer part is rich in iron and calcium, the middle part is iron-rich, and the bottom part contains iron, chromium and nickel. Combining the results from SEM/EDX and the XRD (see Table 2) makes it possible to attribute the upper iron-calcium-rich oxide to $\text{Ca}_2\text{Fe}_2\text{O}_5$. Similarly, it is believed that the middle, iron-rich oxide consist mostly of Fe_2O_3 , while the bottom part of the scale is made up of $(\text{Fe,Cr,Ni})_3\text{O}_4$. It should be noted that the bottom spinel oxide layer is thinner than the corresponding oxide formed adjacent to the former salt agglomerate. This may indicate that the top $\text{Ca}_2\text{Fe}_2\text{O}_5$ layer acts as a protective barrier.

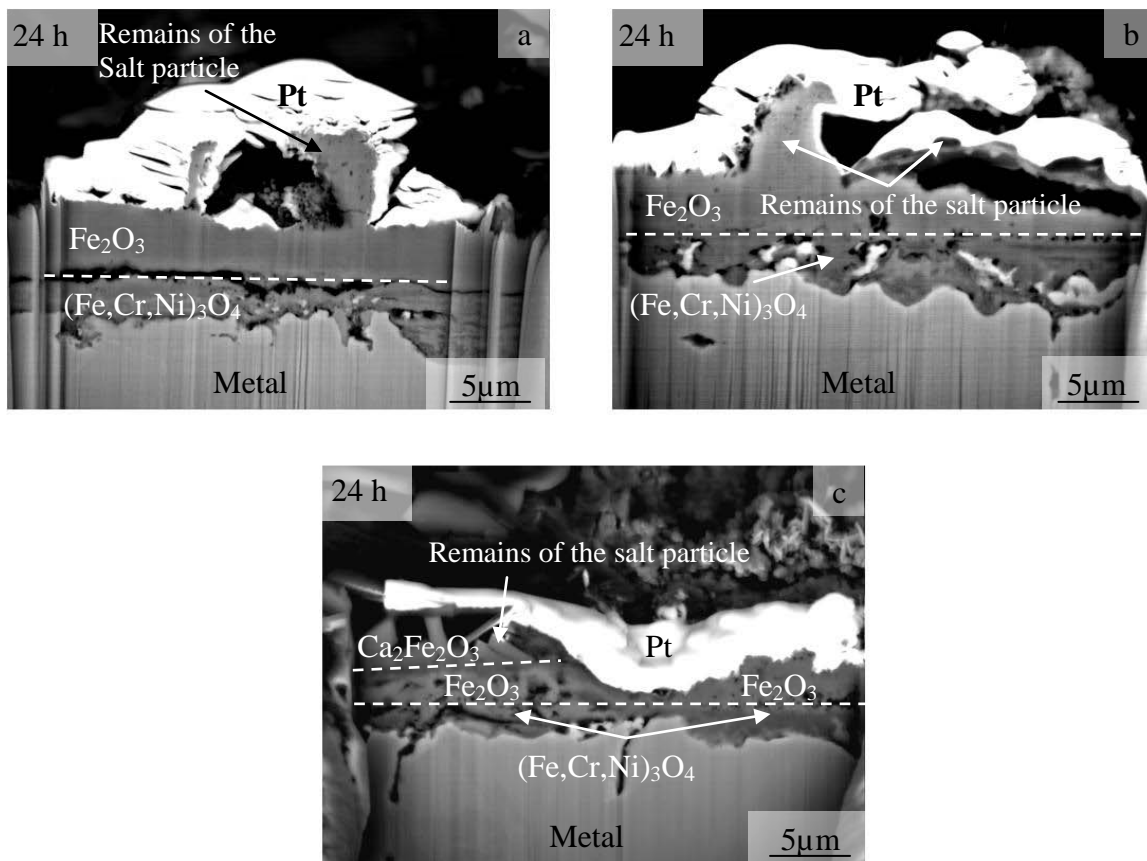


Figure 24. EDX images of FIB cross sections of the remains of a salt particle on a 304L sample exposed for 24 hours in 5% O_2 + 40% H_2O in the presence of (a) KCl, (b) NaCl, (c) CaCl_2 at 600°C .

6.1.2. The effect of SO₂

The results from the salt exposures show that both KCl and NaCl are corrosive towards 304L at 600°C in a wet atmosphere. An explanation for the corrosive behaviour of alkali chlorides towards stainless steels is the formation of alkali chromates. A way to mitigate the corrosive effect of alkali chlorides is to transform the corrosive salts into a less corrosive compound. Previous laboratory studies of 304L at 600°C show that the presence of K₂SO₄ does not induce any accelerated corrosion attack [36]. The noncorrosive nature of K₂SO₄ at this temperature is attributed to its reluctance to react with the protective oxide. Hence, it is possible to transform corrosive alkali chlorides into less corrosive alkali sulphates by adding sulphur dioxide (SO₂) to the flue gas. Thus, corrosive alkali chloride can be converted into less corrosive alkali sulphate.

To understand the effect of SO₂, it is important to investigate the effect in the absence of alkali chlorides. Figure 25 shows the mass gain versus time for samples exposed in 5% O₂ + 40% H₂O + 300ppm SO₂ at 600°C. Reference exposures in O₂ and 5% O₂ + 40% H₂O are also included. The results clearly show that the presence of 300 ppm SO₂ strongly decreases the mass gain of 304L at 600°C in 40% H₂O.

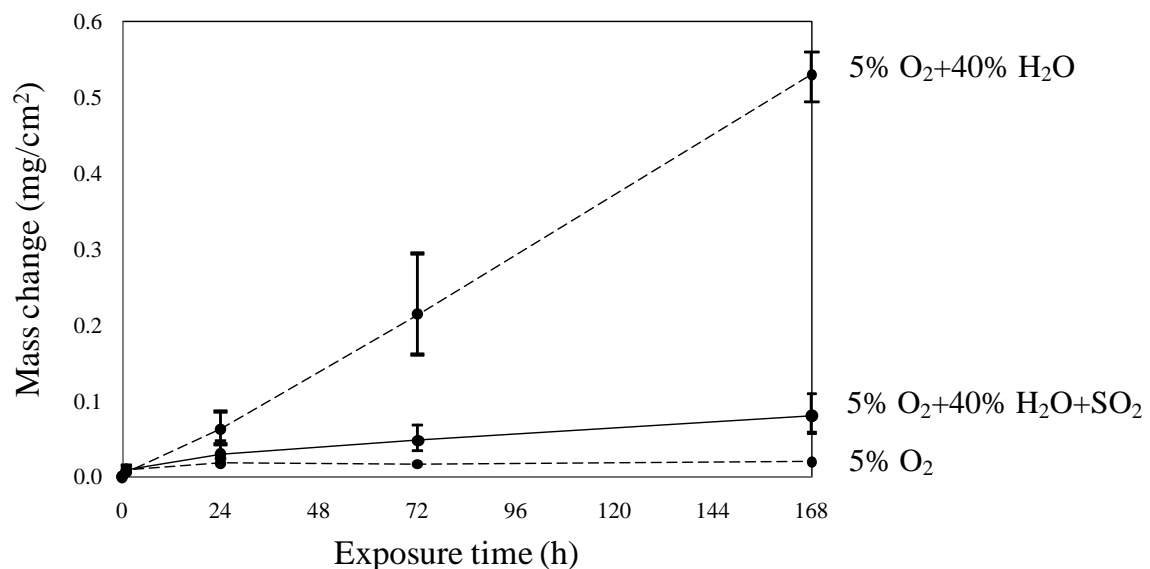


Figure 25. Mass gain versus exposure time for 304L samples exposed in O₂ + 40% H₂O + 300 ppm SO₂ at 600°C. Reference exposures in O₂ and O₂ + 40% H₂O are also included.

Figure 26 shows SE images of samples exposed in (a) wet atmosphere and in (b) wet atmosphere together with 300 ppm SO₂, both for 168 hours of exposure at 600°C. The sample exposed in the absence of SO₂ exhibits a severely corroded surface with island-like features. The samples exposed in the presence of SO₂ exhibit similar corrosion morphology, including oxide islands. However, the islands formed in the presence of SO₂ appear much thinner, which is in accordance with the mass gains recorded.

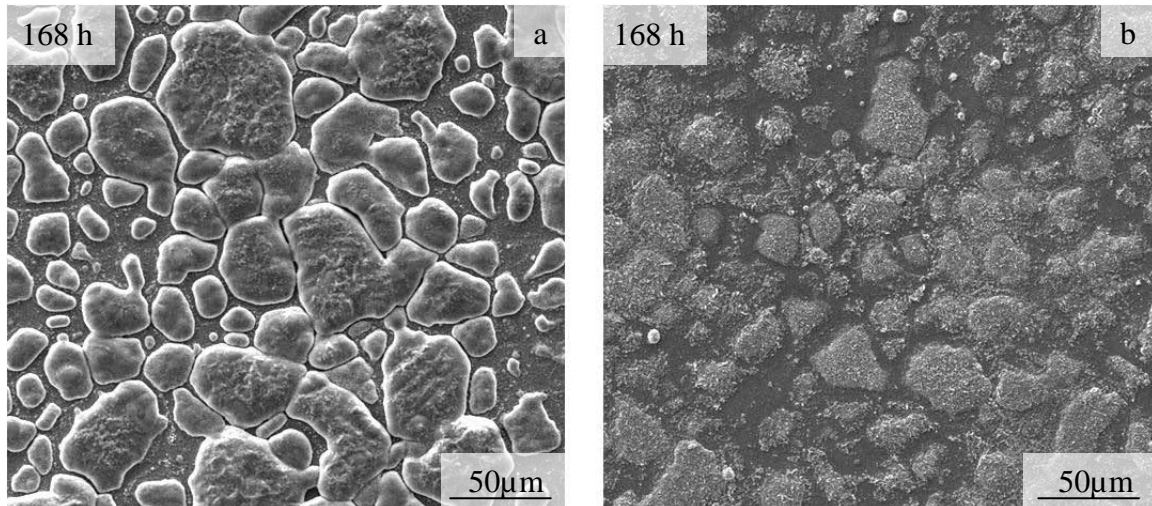


Figure 26. SE images of 304L samples exposed in (a) 5% O₂ and 40% H₂O and (b) 5% O₂ and 40% H₂O + 300 ppm SO₂ for 168 hours at 600°C.

To measure the oxide thickness, cross sections were made through the edge of an oxide island on both samples after 168 hours of exposure, see Figure 27(a and b). In the absence of SO₂ an 8 µm thick layered oxide island has formed. As previously mentioned, the oxide islands consists of outward growing Fe₂O₃ and inward growing (FeCrNi)₃O₄. In the presence of SO₂, the thickness of the oxide scale is about 1 µm. In similarity to exposures in the absence of SO₂, the oxide is layered and consist of an outer iron rich layer, presumably Fe₂O₃, and an inner layer containing iron, chromium and nickel, presumably (Fe,Cr,Ni)₃O₄.

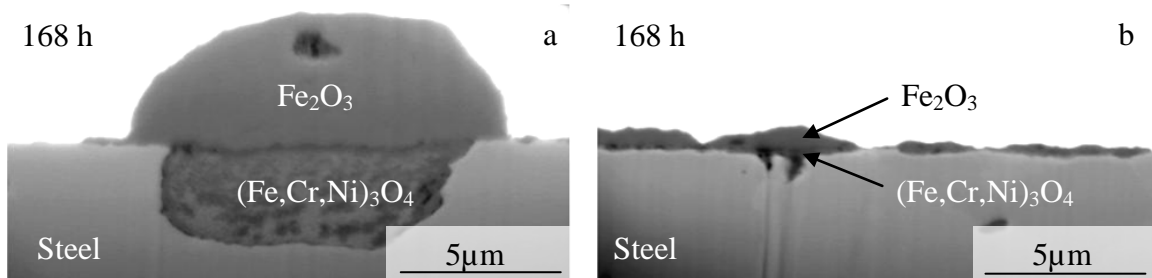


Figure 27. BSE images of FIB cross sections of an oxide island formed on a 304L sample exposed for (a) 5% O₂ and 40% H₂O and (b) 5% O₂ and 40% H₂O + 300 ppm SO₂ for 168 hours at 600°C.

According to the results, SO₂ has a mitigating effect on the oxidation rate. An IC analysis of the sample exposed in the presence of SO₂ detected small amounts of sulphate. It is suggested that this mitigating effect can be attributed to the small amounts of sulphate detected by the IC analysis. In accordance with previous studies, sulphate is believed to be adsorbed at the scale/gas interface [41]. The adsorbed sulphate has been suggested to slow down chromium volatilization and to decrease the rate of oxygen reduction on the oxide surface. While the first effect should postpone the transition to breakaway oxidation, the second effect is expected to slow down the rate of scale growth after breakaway.

The effect of SO₂ on KCl treated samples is presented in the mass gain curve in Figure 28. The results show that the presence of SO₂ decreases the mass gain of KCl treated samples considerably. After 24 hours of exposure, the mass gain amounts to about 40% of the mass gain in the absence of SO₂. However, SO₂ has a minor effect on the slope of the mass gain curve during later stages.

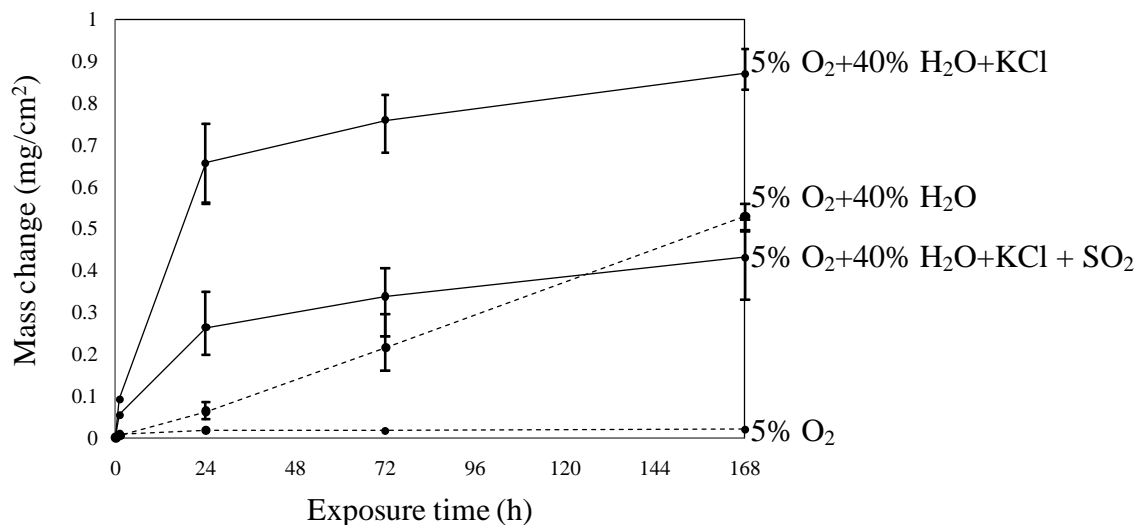


Figure 28. Mass gain versus exposure time for 304L samples exposed in O₂ + 40% H₂O + KCl and O₂ + 40% H₂O + 300 ppm SO₂ at 600°C. Reference exposures in O₂ and O₂ + 40% H₂O are also included.

Corrosion products formed during the salt exposures were analyzed with XRD and IC. The IC analysis did not show any signs of chromate formation. Instead, high amounts of sulphate were detected. The IC analysis was in agreement with the XRD analysis (Table 3); no potassium chromate was detected. Instead, potassium sulphate (K_2SO_4) and potassium manganese sulphate ($K_2Mn_2(SO_4)_3$) were detected, which indicates that the presence of SO_2 prevents the chromate formation by the transformation of KCl to K_2SO_4 . Furthermore, both Fe_2O_3 and Me_3O_4 was detected which shows that an iron rich oxide has started to form. However, medium intensity diffraction from the steel substrate indicates that the oxide is still thin.

Table 3. Crystalline phases detected by XRD on KCl treated 304L samples for 24 hours in the presence of SO_2 . Exposures in the absence of SO_2 are also included.

	Salt	304L	Fe_2O_3	Me_3O_4	K_2CrO_4	K_2SO_4	$K_2Mn_2(SO_4)_3$
KCl + SO_2:	–	M	S	W	–	M	W
KCl:	–	–	S	W	W	–	–

S= Strong intensity, M = Medium intensity, W = Weak intensity

A BSE image together with EDX maps of the KCl treated sample exposed in the presence of SO_2 for 24 hours is shown in Figure 29. The surface is covered by a Fe-rich oxide. No unreacted salt or chlorine is detected in the remains of the salt particle or on the oxide surface. Potassium can be detected in areas correlating to sulphur and oxygen. Identification of K_2SO_4 was made by XRD. Hence, these particles are attributed to K_2SO_4 .

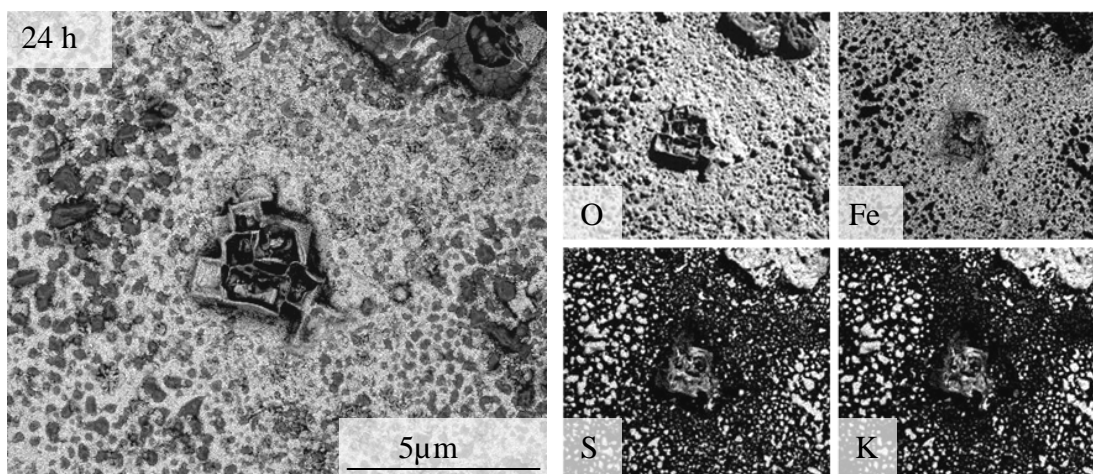
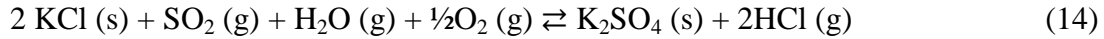


Figure 29. EDX images of a sample exposed for 24 hours in presence of KCl at 600°C in 5% O_2 + 40% H_2O + 300 ppm SO_2 .

The K_2SO_4 rich areas can be detected, not only in the remains of the salt particle, but also on the oxide between the salt particles. Therefore, it is proposed that KCl diffuses out from the salt particle and reacts with the atmosphere, forming K_2SO_4 :



Due to the noncorrosive nature of K_2SO_4 at this environment and temperature, it does not deplete the oxide in chromium. In addition, sulphate from $\text{SO}_2(\text{g})$ will be adsorbed on the surface. As previously mentioned, it is suggested that adsorbed sulphate slows down chromium volatilization and decreases the rate of oxygen reduction on the oxide surface.

Backscattered electron images of BIB cross sections of KCl treated samples exposed in (a) the absence of SO_2 and in (b) the presence of SO_2 after 168 hours of exposure are shown in Figure 30. The cross sections were cut through the surface between the remains of the salt particles. In the absence of SO_2 , a thick oxide scale has formed; up to 11 μm in thickness. The oxide formed in the presence of SO_2 shows a morphology similar to that of the sample exposed in the absence of SO_2 (see Section 6.1). Thus, a two-layered oxide scale has formed, consisting of an outward Fe_2O_3 , and an inward layer containing iron, chromium and nickel, presumably $(\text{Fe,Cr,Ni})_3\text{O}_4$. The oxide is thinner; it has an average thickness of about 4 μm .

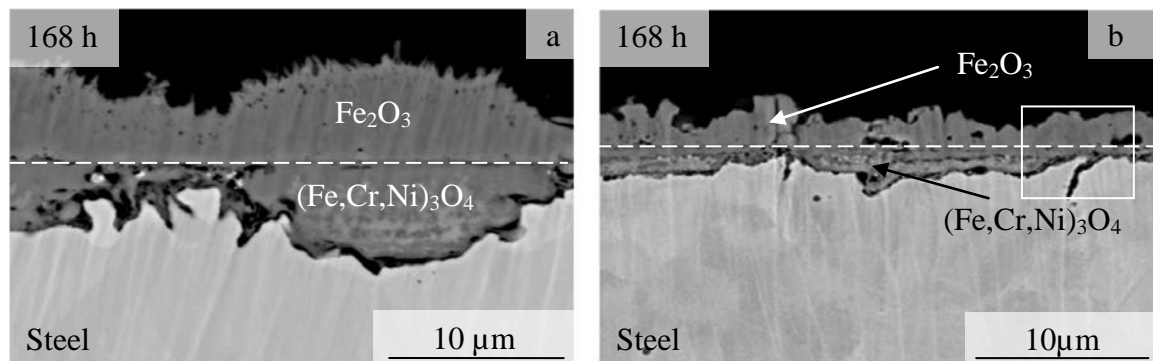


Figure 30. BSE image of BIB cross section samples exposed in (a) 5% O_2 + 40% H_2O + KCl and (b) in 5% O_2 + 40% H_2O + KCl SO_2 for 168 hours. BSE image of the selected area in (b) together with EDX maps in higher magnification is shown in Figure 31.

The presence of SO_2 on KCl treated samples results in a slower oxide growth than for KCl treated samples exposed in the absence of SO_2 . However, the oxide on samples exposed in KCl + SO_2 for 168 hours is about four times thicker than to the samples exposed in SO_2 for 168 hours; compare Figure 27(a) and Figure 30(b). Thus, it seems that KCl may have a corrosive effect despite the presence of SO_2 . A proposal is that small amounts of the unreacted KCl may initially react with the protective oxide and, by chromate formation, deplete the oxide in chromium. The depletion leads to the formation of a non-protective iron rich oxide. However, because of the presence of SO_2 , K_2CrO_4 will immediately react with SO_2 to form K_2SO_4 . Thus, no potassium chromate can be detected.

Another problem with $\text{SO}_2(\text{g})$ is the possible formation of metal sulphides.

Figure 31 shows a close up BSE image of the selected area in Figure 30(a) together with EDX maps. According to the images, sulphur can be detected, not only in the oxide/gas interface, but also in the crack formed under the oxide scale (marked with arrows). In the oxide/gas interface, sulphur correlates to potassium and can be recognized as K_2SO_4 . This correlation cannot be seen in the crack. This suggests the formation of metal sulphides. Sulphidizing is bad from a corrosion point of view because of the high oxidation rate in sulphides compared with those in oxide. The higher oxidation rate is attributed to the faster outward diffusion of cations through the sulphides of iron, nickel and chromium [16]. Furthermore, it is suggested that the presence of metal sulphides decreases the scale adhesion which induces spallation of the oxide layer. However, the presence of metal sulphides is relatively low. Thus, the overall effect of sulphur is considered to be positive under these experimental conditions.

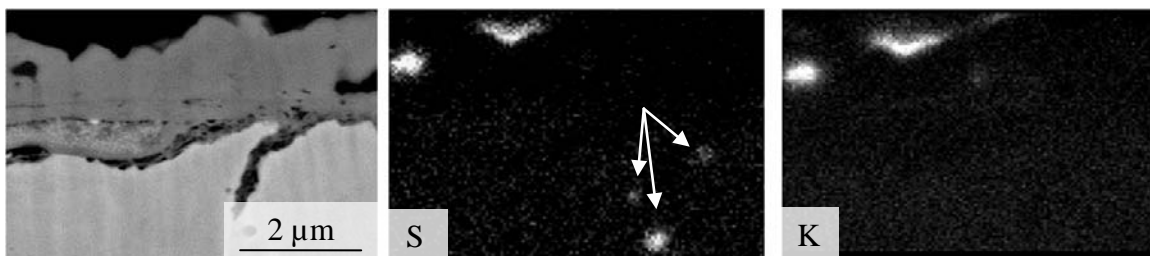


Figure 31: BSE image together with EDX maps of the area marked in Figure 30b.

6.1.3. Summary of laboratory exposures

- 304L forms a chromium rich oxide of corundum type, $(\text{Cr,Fe})_2\text{O}_3$ when exposed in a dry atmosphere at 600°C . The oxide protects the steel and further oxidation continues at a slow rate.
- Water vapour reacts with the chromium rich oxide, forming volatile chromic acid, $\text{CrO}_2(\text{OH})_2(\text{g})$. The process depletes the oxide in chromium; oxide island forms at the centre of the steel grains where the chromium supply is low. The oxide islands consist of an outward growing hematite, Fe_2O_3 , and an inward growing spinel type oxide, $(\text{Fe,Cr,Ni})_3\text{O}_4$. This two-layered scale is expected to be poorly protective and permeable for oxide and chloride ions, resulting in an accelerated corrosion rate.
- Potassium chloride (KCl) and sodium chloride (NaCl) increase the corrosion rate by alkali chromate (K_2CrO_4 and Na_2CrO_4) formation. In similarity to the corrosion attack induced by water vapour, the protective properties of the chromium rich oxide are lost due to chromium depletion. In contrast, the presence of KCl and NaCl causes breakaway corrosion all over the sample surface.
- Calcium chloride (CaCl_2) may also deplete the protective oxide by chromate formation (CaCrO_4). However, under the laboratory conditions chosen, CaCl_2 is rapidly converted to calcium oxide (CaO). Due to the poor mobility of CaO, Ca does not spread over the surface and the reaction between Ca and the protective oxide is limited.
- The corrosion rate can be limited by adding sulphur dioxide (SO_2) to the flue gas.
- In water vapour the effect of SO_2 is attributed to the formation of adsorbed sulphate on the oxide surface. The adsorbed sulphate is suggested to slow chromium volatilization and to decrease the rate of oxygen reduction on the oxide surface.

- In an O_2+H_2O+KCl environment the mitigated corrosion effect of SO_2 is mainly attributed to the conversion of KCl to potassium sulphate (K_2SO_4). In contrast to KCl , K_2SO_4 does not deplete the protective oxide in chromium by forming K_2CrO_4 .
- The presence of SO_2 may result in the formation of metal sulphides. Sulphidizing increases the oxidation rate because of the faster outward diffusion of cations through the sulphides of iron, nickel and chromium. It is also suggested that the presence of metal sulphides decreases the scale adhesion which induces spallation of the oxide layer.

6.2. Field exposures

As previously mentioned, burning waste and biofuels results in a corrosive flue gas relatively rich in alkali chloride. In addition, the sulphur dioxide content is relatively low. Consequently, the deposit formed on the superheater tubes, for example, tends to be rich in corrosive alkali chloride. The results in Section 6.1 showed that KCl and $NaCl$ are corrosive towards stainless steels, primarily because of alkali chromate formation. By adding SO_2 to the gas flow, the corrosive alkali chlorides were converted into the corresponding and less corrosive alkali sulphates. Therefore, by increasing the available sulphur in the boiler, corrosive alkali chloride in the deposits may be converted in the same way, i.e. into less corrosive alkali sulphates. The availability of sulphur can be increased by using sulphur rich-fuel additives. Municipal sewage sludge contains sulphur in the form of sulphates. In addition, municipal sewage sludge also contains phosphorus and alumina silicates, all with the ability to react with alkali chlorides.

6.2.1. The effect of municipal sewage sludge

To investigate the effect of municipal sewage sludge, a reference exposure without additives was also included. In the reference exposure (denoted RDF) bark pellets were co-fired with waste (refuse derived fuel) pellets. The share of waste was 22% based on the total amount of dry fuel supplied to the boiler. By adding sewage sludge (13% calculated on dry weight) to the reference fuel (denoted RDF-13%HIM), the content of gaseous alkali chloride content was reduced from 96 ppm to 3 ppm. In contrast, the $SO_2(g)$ increased from 3 ppm to 69 ppm [6, 42].

In both exposures (RDF and RDF-13%HIM) two materials, 304L and Sanicro 28, were exposed for 24 hours. The material temperature was kept at 600°C.

Figure 32 shows the sample rings after exposure. In the RDF case, both 304L and Sanicro 28 are covered by a thick, brownish deposit. The deposit layer formed on the 304L sample ring appears to be more prone to spallation than the deposit formed on Sanicro 28. For the RDF-13%HIM case, the samples are covered by a reddish deposit. The red colour is due to high levels of iron in the sludge added. Metallic lustre can be seen on the samples, especially on the Sanicro 28 sample, which indicates a thinner deposit layer than on the RDF exposure.

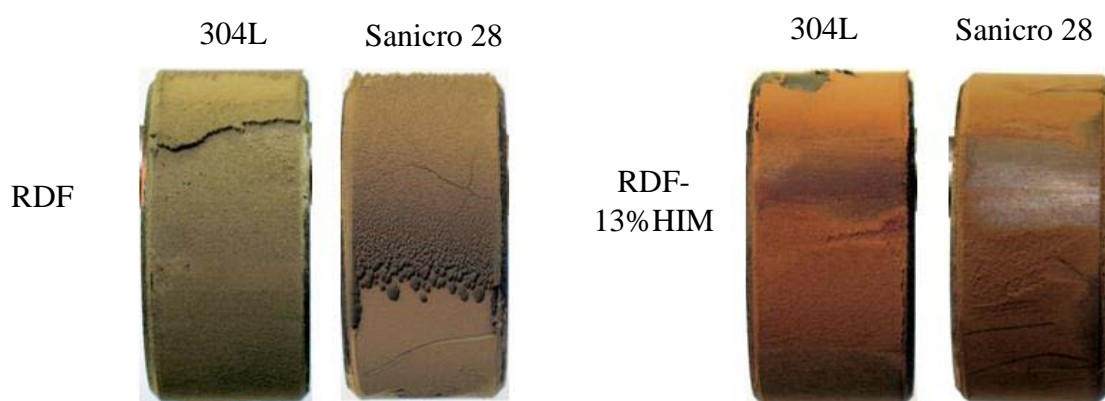


Figure 32: Optical images of the corrosion probe samples exposed for 24 hours at 600°C.

In order to analyze the samples after exposure, three analytical methods were used: SEM/EDX, XRD and IC. For the Sanicro 28 sample rings, the deposit was mechanically removed. Crystalline corrosion products were analyzed with XRD. After the XRD analysis, the deposit was leached in MilliQ water for quantification of the amount of water soluble chlorine and sulphate ions with IC. The 304L sample rings were mounted in epoxy and cut in order to get a cross section in which the deposit, oxide layer and metal could be analysed with SEM/EDX.

The IC analysis of the RDF sample showed that the deposit was dominated by chloride ions. Just a few percent of the ions were detected as sulphate ions. The XRD analysis of the deposit showed similar results and high intensity diffraction from KCl and NaCl was detected. Hence, the results clearly indicate that the deposit formed in the RDF environment is rich in alkali chloride. In the RDF-13%HIM case, the deposit was totally

dominated by sulphate ions while the amounts of chlorine decreased to a level near the detection limit. The IC results were in agreement with XRD; no alkali chlorides were detected. Instead, strong diffractions from calcium sulphate (CaSO_4), potassium calcium sulphate ($\text{K}_2\text{Ca}_2(\text{SO}_4)_3$), potassium aluminum silicate (KAlSi_2O_6) and potassium calcium iron phosphate ($\text{KCaFe}(\text{PO}_4)_2$) were detected, which supports the theory that alkali chloride may be transformed by the addition of municipal sewage sludge.

Figure 33 shows BSE images of the cross section of the 304L ring together with EDX maps from the RDF case. Four distinctive areas can be identified; (1) the steel sample ring, (2) the corrosion product layer, (3) the deposit layer and (4) the epoxy. The thickness of the oxide layer varies between 30 μm to 100 μm , and the thickness of the covering deposit layer is from 550 μm to 600 μm thick. In agreement with IC and XRD a layer rich in KCl can be detected. According to the laboratory results, KCl reacts with the protective oxide that is initially formed on 304L and then forms potassium chromate, see reaction (8). The reaction depletes the oxide in chromium and a duplex, poorly protective, scale forms. The EDX maps show that the corrosion product layer has a morphology similar to the laboratory exposure with KCl and NaCl, see Figure 24 (a) and (b), i.e. the oxide is layered. The outer layer, dominated by iron oxide, is probably outward growing. The inner layer is iron and chromium rich and is probably present as an inward growing spinel type oxide. However, no alkali chromate was detected, which would be expected according reaction (8). In addition, nodules of almost pure chromium oxide (Cr_2O_3) could be seen embedded in the outward growing iron rich oxide. In the laboratory, the oxide formed on 304L under mild conditions consists of a solid solution of Cr and Fe. Therefore, it is not expected that this pure chromia could have formed from oxidation of the steel. Instead, the nodules are probably a result of decomposition of alkali chromate. It is suggested that the initial formation of alkali chromate on the oxide surface decompose to chromium oxide and alkali hydroxide in reducing environment. Nevertheless, chromium has been depleted from the protective oxide initially formed. Thus, the protective oxide was transformed into a poorly protective and fast growing Fe_2O_3 oxide.

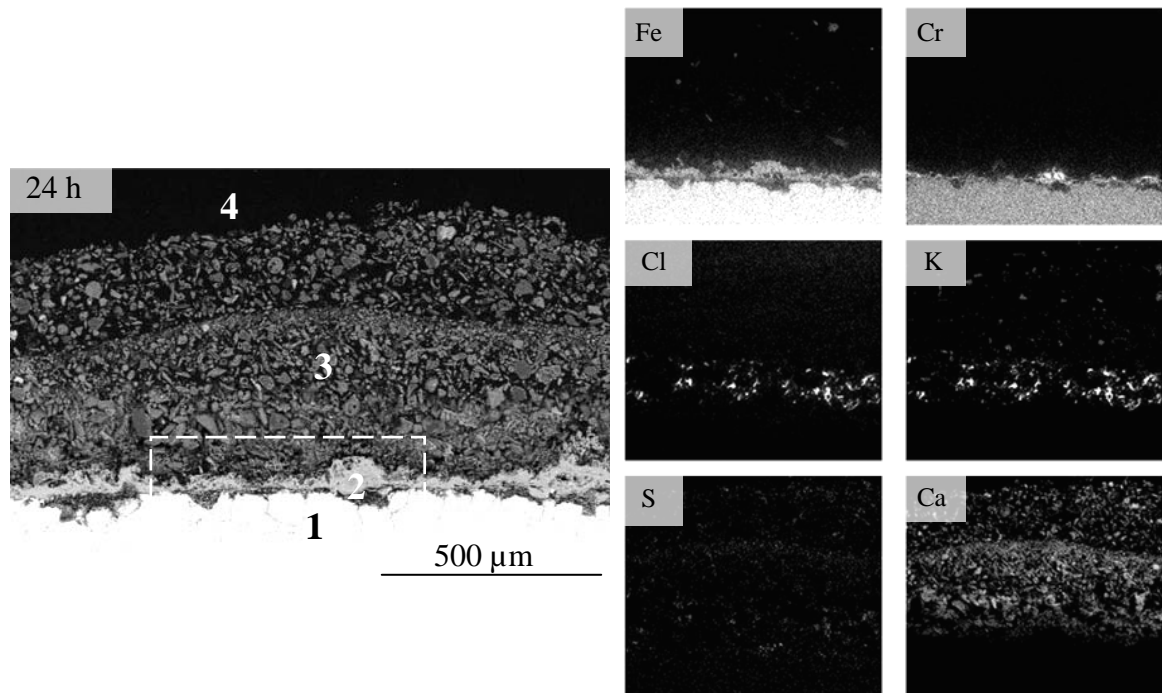


Figure 33: BSE image, together with EDX maps, of a cross section of the 304L sample exposed in the RDF case for 24 hours at 600°C. BSE image of the area marked is shown in higher magnification in Figure 34.

Due to the poor protection of the oxide scale, the underlying steel may be attacked. Figure 34 shows a close up picture of the selected area in Figure 33. High void concentration can be seen in the inner part of the oxide scale as well as internal oxidation along the steel grain boundaries.

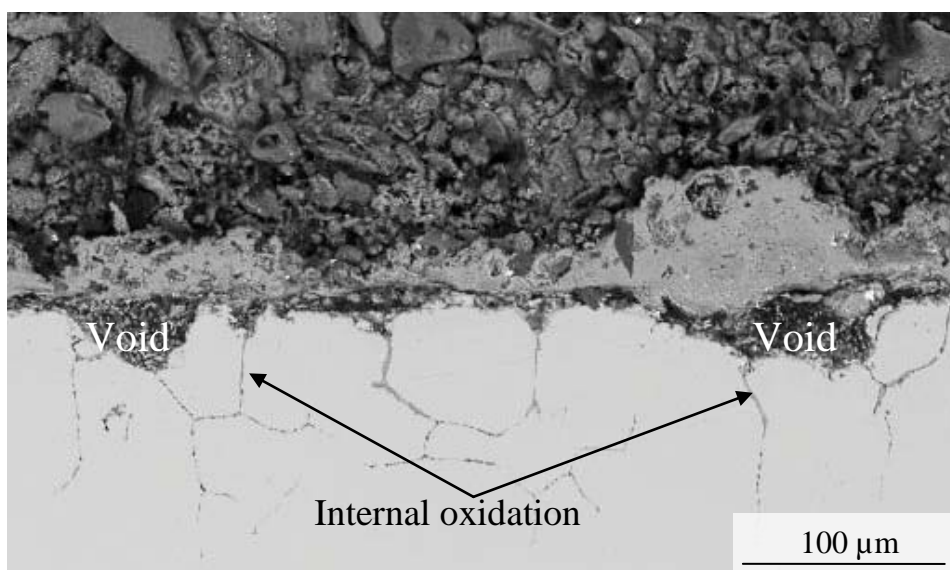


Figure 34: BSE image of the marked area in Figure 33.

As shown in Section 6.1, reactions by which alkali chlorides are converted into less aggressive alkali sulphates are beneficial from a corrosion point of view. Municipal sewage sludge contains high levels of sulphur, phosphorus and aluminosilicates, all with the ability to react with alkali chlorides.

Figure 35 shows a BSE image of the cross section from the RDF-13%HIM sample together with EDX maps from the marked area in the BSE image. In agreement with IC and XRD, no alkali chloride is detected with EDX. Instead, the deposit layer consists of a porous network of individual particles, 10–50 μm in size. The particles have three types of composition: calcium sulphur and oxygen, potassium, calcium, iron, phosphorus and oxygen and potassium, alumina, silica and oxygen. According to XRD, it is proposed that these areas are CaSO_4 , $\text{KCaFe}(\text{PO}_4)_2$ and KAlSi_2O_6 . No corrosion product layer can be seen beneath the deposit layer. Thus, the oxide formed on the sample is in the submicron range, probably less than 0.3 μm in thickness. Furthermore, there are no signs of internal oxidation in the steel grain boundaries. Hence, the addition of municipal sewage sludge is believed to reduce the presence of corrosive alkali chlorides by reacting with sulphur (reaction 14), phosphorous and alumina silicates, in the gas phase or on particles.

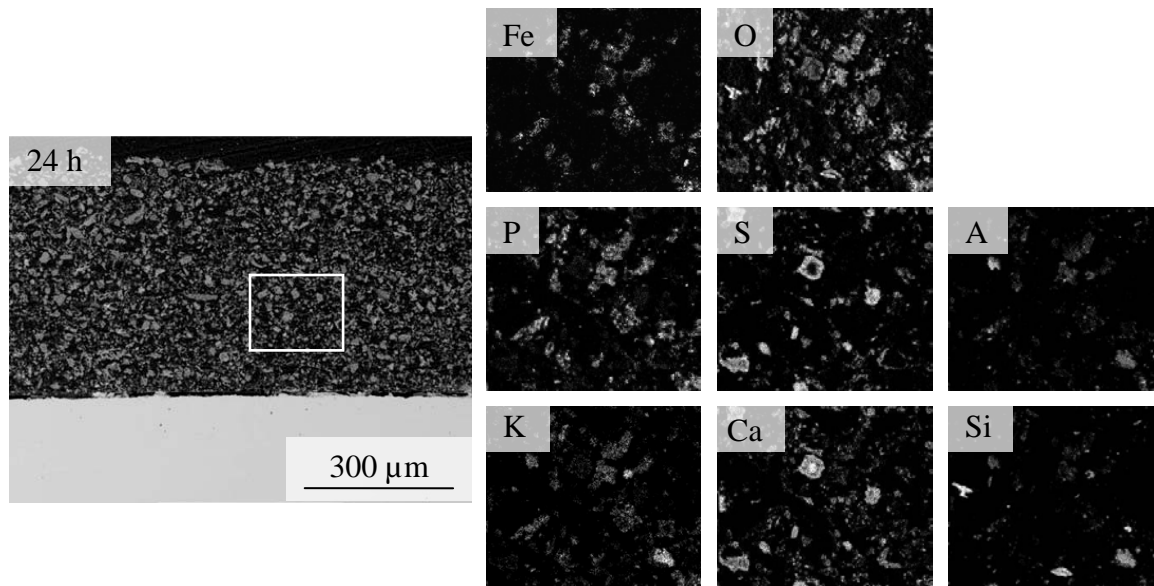


Figure 35: BSE image, together with EDX maps, of a cross section of the 304L sample exposed in the RDF-13%HIM case for 24 hours at 600°C. BSE image of the cross section from the RDF-13%HIM sample together with EDX maps of the area marked in the BSE image.

6.2.2. Summary of field exposures

- The RDF exposure resulted in a flue gas containing high levels of gaseous alkali chlorides (96ppm) and a low level of SO₂(g) (3ppm).
- Without additives a thick oxide scale was formed on the samples, covered by a deposit in which a large amount of corrosive alkali chlorides were detected.
- The addition of municipal sewage sludge reduced the amount of gaseous alkali chlorides in the flue gas to 3 ppm and increased the amount of SO₂(g) to 69 ppm.
- The change in flue gas chemistry resulted in a transformation of the corrosive alkali chlorides into less corrosive alkali compounds, i.e. alkali sulphates, alkali phosphates and alkali aluminum silicates. As a result, the corrosion rate was significantly decreased.

7. Conclusions

The presence of KCl and NaCl strongly accelerates the high temperature corrosion of 304L stainless steel in a 5%O₂ + 40%H₂O environment. The corrosion is initiated by the formation of alkali chromate through the reaction of alkali with the protective oxide. Chromate formation is a sink for chromium in the oxide; this leads to a loss of its protective properties. Subsequently, a rapidly growing scale forms, consisting of an outer hematite layer and an inner layer of spinel oxide, (Fe,Cr,Ni)₃O₄. In contrast to NaCl and KCl, CaCl₂ is not very corrosive under the exposure conditions used here. This is because CaCl₂ is rapidly converted to CaO. Due to the poor mobility of CaO, only small amounts of CaCrO₄ form where CaO is in direct contact with the scale. CaO also reacts with the scale to form Ca₂Fe₂O₅. The addition of 300 ppm SO₂ mitigates the rapid oxidation of 304L in the O₂ + H₂O environment, in both the absence and presence of KCl. In the absence of KCl, the effect of SO₂ is attributed to the formation of adsorbed sulphate on the oxide surface. The adsorbed sulphate is believed to slow chromium volatilization and to decrease the rate of oxygen reduction on the oxide surface. In an O₂ + H₂O + KCl environment, the corrosion mitigating effect of SO₂ is mainly attributed to the conversion of KCl to K₂SO₄. In contrast to KCl, K₂SO₄ does not deplete the protective oxide in chromium by forming K₂CrO₄. As in the absence of KCl, adsorbed sulphate is suggested to slow chromium volatilization and to decrease the rate of oxygen reduction on the oxide surface.

The addition of municipal sewage sludge to the 12-MWth CFB boiler at Chalmers University of Technology resulted in a reduced corrosion rate of 304L and Sanicro 28 at 600°C after 24 hours of exposure. Without additives, a thick oxide scale was formed on the samples, covered by a deposit rich in corrosive alkali chlorides. Adding digested sewage sludge to the fuel reduced the corrosion rate. The steel ring was protected by a thin oxide, covered by a deposit rich in less corrosive alkali sulphates, alkali phosphates and alkali aluminum silicate.

8. Acknowledgements

First of all I would like to thank my supervisors: Professor Jan-Erik Svensson, Professor Lars-Gunnar Johansson and Jesper Liske, Ph. D., for the support and for all the knowledge you have shared with me. Special thanks go to Jesper who always had time for questions and interesting discussions.

I am also grateful to Professor Oliver Lindquist for giving me the opportunity to do research at Environmental Inorganic Chemistry, Chalmers.

Moreover, I would like to acknowledge the High Temperature Centre (HTC), Konsortiet för Materialteknik för termiska energiprocesser (KEM), Värmeforsk (VF) and the Swedish Energy Agency (STEM), with their member companies, for support and funding.

Sincere thanks go also to Torbjörn Jonson, Ph. D., for his support during the latter part of my research and to my office mate, Kristina Hellström, Ph. D., for the nice atmosphere in room 6069. I would also like to thank my other colleagues, both former and present, in the corrosion research group: Josefin Engkvist, Ph.D., Maria Nikumaa, Niklas Israelsson, Rakshith Sachitanand, Jan Froitzheim, Ph. D., Sead Canovic, Ph. D., Professor Mats Halvarsson, Nicklas Folkesson, Ph. D., Carolina Pettersson, Ph. D., and Linda Ingemarsson, Ph. D., for making it so pleasant to work here. Furthermore, I want to thank Associate Professor Lars-Erik Åmand at the Department of Energy and Environment for support and nice collaboration.

I would also like to thank Anders Kvist, Ph. D., for support in the Microscopy, Professor., Vratislav Langer for support with X-ray diffraction, Charlotte Bouveng for assistance with administrative matters, Esa Väänänen for technical support, and Roger Sagdahl for help with computers and electronics.

Finally, I would like to thank my partner Erik for all his support with everything ♥.

9. Reference List

1. Metz, B., Davidson, O., de Coninck, H. C., Loos, M., Meyer, L.A., *IPCC Special Report on Carbon Dioxide Capture and Storage. Prepared by Working Group III of the Intergovernmental Panel on Climate Change*, Cambridge University Press, Cambridge, (2005).
2. Wigler, A. Personal communication. E.ON (An energy supplier), Norrköping, Sweden. (August 2011).
3. Jenkins, B.M., Baxter, L. L., Miles, T. R., Combustion properties of biomass. *Fuel Processing Technology*, (1998), **54**(1–3), pp. 17–46.
4. Davidsson, K.O., Åmand, L.-E., Leckner, B., Kovacevik, B., Svane, M., Hagström, M., Pettersson, J. B. C., Pettersson, J., Asteman, H., Svensson, J.-E., Johansson, L.-G., Potassium, Chlorine, and Sulfur in Ash, Particles, Deposits, and Corrosion during Wood Combustion in a Circulating Fluidized-Bed Boiler. *Energy & Fuels*, (2007), **21**(1), pp. 71–81.
5. Pettersson, J., Pettersson, C., Folkesson, N., Johansson, L.-G., Skog, E., Svensson, J.-E., The influence of sulphur additions on the corrosive environment in a waste-fired CFB boiler. *Materials Science Forum*, (2006), **522–523**, pp. 563–570.
6. Karlsson, S., Pettersson, J., Åmand, L.-E., Reducing high temperature corrosion when burning waste by adding digested sewage sludge. In: *Swedish/Finnish Flame Days*. (January 26–27, 2011). The Swedish and Finnish National Committees of the International Flame Research Foundation. Piteå, Sweden.
7. Folkesson, N., Pettersson, J., Pettersson, C., Johansson, L.-G., Skog, E., Andersson, B.-Å., Enestam, S., Tuiremo, J., Jonasson, A., Heikne, B., Svensson, J.-E., Fireside corrosion of stainless and low alloyed steels in a waste-fires CFB boiler: The effect of adding sulphur to the fuel. *Materials Science forum*, (2008), **595-598**, pp. 289–297.
8. Grabke, H.J., Reese, E., Spiegel, M., The effects of chlorides, hydrogen chloride, and sulfur dioxide in the oxidation of steels below deposits *Corrosion Science*, (1995), **37**(7), pp. 1023–43.
9. Michelsen, H.P., Frandsen, F., Dam-Johansen, K., Larsen, O. H., Deposition and high temperature corrosion in a 10 MW straw fired boiler *Fuel Processing Technology*, (1998), **54**(1–3), pp. 95–108.
10. Montgomery, M., Karlsson, A., In-situ corrosion investigation at Masnedø CHP plant – A straw-fired power plant. *Materials and Corrosion*, (1999), **50**(10), pp. 579–584.
11. Nielsen, H.P., Frandsen, F. J., Dam-Johansen, K., Lab-Scale Investigations of High-Temperature Corrosion Phenomena in Straw-Fired Boilers. *Energy & Fuels*, (1999), **13**(6), pp. 1114–1112.
12. Pettersson, J., *Alkali Induced High Temperature Corrosion of Stainless Steel - Experiences from Laboratory and Field*, in *Department of Chemical and Biological Engineering*. 2008, Chalmers University of Technology: Gothenburg. p. 84.
13. Kofstad, P., *High Temperature Corrosion*, Elsevier Applied Science, London, (1988). pp. 558.
14. Jones, D.A., *Principles and Prevention of Corrosion*, 2 edn., Prentice Hall, New Jersey, (1995). pp. 572.
15. Wagner, C., Beitrag zur Theorie des Anlaufvorgangs. *Zeitschrift für Physikalische Chemie*, (1933), **B21**, pp. 25–41.
16. Khanna, A.S., *Introduction to High Temperature Oxidation and Corrosion*, ASM International, Delhi, (2002). pp. 325.

17. Honeycombe, R.W.K., Bhadeshia, H. K. D. H., *Steels: Microstructure and Properties*, 2 edn., Butterworth-Heinemann, Oxford, (1995). pp. 324.
18. Callister Jr, W.D., *Materials Science and Engineering: An Introduction*, 5th edn., John Wiley & Sons, New York, (1999).
19. Briks, N., Meier, G. H., Pettit, F. S., *Introduction to the High Temperature Oxidation of Metals*, 2 edn., Cambridge University Press, Cambridge, (2006). pp. 352.
20. Asteman, H., Svensson, J.-E., Johansson, L.-G., Norell, M., Indication of Chromium Oxide Hydroxide Evaporation During Oxidation of 304L at 873 K in the presence of 10 % Water Vapor. *Oxidation of Metals*, (1999), **52**(1–2), pp. 95–111.
21. Asteman, H., Svensson, J.-E., Norell, M., Johansson, L.-G., Influence of Water Vapor and Flow Rate on the High-Temperature Oxidation of 304L; Effect of Chromium Oxide Hydroxide Evaporation *Oxidation of Metals*, (2000), **54**(1–2), pp. 11–26.
22. Asteman, H., Segerdahl, K., Svensson, J.-E., Johansson, L.-G., The Influence of Water Vapor on the Corrosion of Chromia-Forming Steels. *Materials Science Forum* (2001), **369–372**, pp. 277–286.
23. Asteman, H., Svensson, J.-E., Johansson, L.-G., Evidence for Chromium Evaporation Influencing the Oxidation of 304L: The Effect of Temperature and Flow Rate. *Oxidation of Metals*, (2002), **57**(3–4), pp. 193–216.
24. Segerdahl, K., Svensson, J.-E., Johansson, L.-G., The high temperature oxidation of 11% chromium steel: Part I – Influence of pH₂O. *Materials and Corrosion*, (2002), **53**(4), pp. 247–255.
25. Segerdahl, K., Svensson, J.-E., Johansson, L.-G., The high temperature oxidation of 11% chromium steel: Part II – Influence of flow rate. *Materials and Corrosion*, (2002), **53**(7), pp. 479–485.
26. Segerdahl, K., Johansson, L.-G., Svensson, J.-E., Protective and Nonprotective Behavior of 11% Cr Steel in O₂ + H₂O Environment at 450–700°C. *Journal of the electrochemical society*, (2004), **151**(7), pp. B394–B398.
27. Montgomery, M., Karlsson, A., Larsen, O. H., Field test corrosion experiments in Denmark with biomass fuels. Part 1: Straw-firing. *Materials and Corrosion*, (2002), **53**(2), pp. 121–131.
28. Nielsen, H.P., Frandsen, F. J., Dam-Johansen, K., Baxter, L. L., The implications of chlorine-associated corrosion on the operation of biomass-fired boilers *Progress in Energy and Combustion Science*, (2000), **26**(3), pp. 283–298.
29. Wang, C.-J., He, T.-T., Morphological development of subscale formation in Fe-Cr-(Ni) alloys with chloride and sulfates coating. *Oxidation of Metals*, (2002), **58**(3–4), pp. 415–437.
30. Folkesson, N., Jonsson, T., Halvarsson, M., Johansson, L.-G., Svensson J.-E., The influence of small amounts of KCl(s) on the high temperature corrosion of a Fe-2.25Cr-1Mo steel at 400 and 500°C. *Materials and Corrosion*, (2011), **62**(7), pp. 606–610.
31. Proff, C., Jonsson, T., Pettersson, C., Svensson, J.-E., Johansson, L.-G., Halvarsson, M., Microstructural investigation of the KCl-induced Corrosion of the Austenitic alloy Sanicro 28 (35Fe27Cr31Ni) at 600°C. *Materials at High Temperature*, (2008), **26**(2), pp. 113–125.
32. Pettersson, J., Asteman, H., Svensson, J.-E., Johansson, L.-G., KCl Induced Corrosion of a 304-type Austenitic Stainless Steel at 600°C; The Role of Potassium. *Oxidation of Metals*, (2005), **64**(1–2), pp. 23–41.

33. Pettersson, C., Johansson, L.-G., Svensson, J.-E., The Influence of Small Amounts of KCl(s) on the Initial Stages of the Corrosion of Alloy Sanicro 28 at 600 °C *Oxidation of metals*, (2008), **70**(5–6), pp. 241–256.
34. Pettersson, C., Pettersson, J., Asteman, H., Svensson, J.-E., Johansson, L.-G., , KCl-induced high temperature corrosion of the austenitic Fe–Cr–Ni alloys 304L and Sanicro 28 at 600 °C *Corrosion Science*, (2006), **48**(6), pp. 1368–1378.
35. Jonsson, T., Froitzheim, J., Pettersson, J., Svensson, J.-E., Johansson, L.-G., Halvarsson, M., The Influence of KCl on the Corrosion of an Austenitic Stainless Steel (304L) in Oxidizing Humid Conditions at 600 degrees C: A Microstructural Study. *Oxidation of Metals*, (2009), **73**(3–4), pp. 213–239.
36. Pettersson, J., Folkesson, N., Svensson, J.-E., Johansson, L.-G. , The Effects of KCl, K₂SO₄ and K₂CO₃ on the High Temperature Corrosion of a 304-type Austenitic Stainless Steel. *Oxidation of Metals*, DOI: 10.1007/s11085-011-9240-z, (2011).
37. West, A.R., *Basic solid state chemistry*, 2nd edn., John Wiley and Sons, Chichester, (1999). pp. 480.
38. Goldstein, J., Newbury, D. E., Echlin, P., Joy, D. C., Romig Jr, A. D., Lyman, C. E., Fiori, C., Lifshin, E., *Scanning Electron Microscopy and X-Ray Microanalysis: A Text for Biologists, Materials Scientists and Geologists* Kluwer Academic/Plenum Publishers, Dordrecht, Netherlands, (1992). pp. 840.
39. Tang, J.E., Halvarsson, M., Asteman, H., Svensson, J.-E., The microstructure of the base oxide on 304L steel. *Micron*, (2001), **32**(8), pp. 799–805.
40. Halvarsson, M., Tang, J.-E., Asteman, H., Svensson, J.-E., Johansson, L.-G., Microstructural investigation of the breakdown of the protective oxide scale on a 304 steel in the presence of oxygen and water vapour at 600°C. *Corrosion Science*, (2006), **48**(8), pp. 2014–2035.
41. Järtnäs, A., Svensson, J.-E., Johansson, L.-G., Influence of SO₂ on the oxidation of 304L steel in O₂+40%H₂O at 600 degrees C. *Oxidation of Metals*, (2008), **69**(3–4), pp. 249–263.
42. Herstad Svärd, S., Steenari, B.-M., Åmand, L.-E., Bowalli, J., Öhlin, J., Pettersson, J., Karlsson, S., Larsson, E., Svensson, J.-E., Johansson, L.-G., Davidsson, K., Bäfver, L., Almark, M. , *Measures for simultaneous minimization of alkali related operating problems, Phase 3*, Värmeforsk, Göteborg, Sweden, (2010).

